International Simple Glass (ISG) dissolution rate in a (Si, Ca)-rich environment at 90 °C and alkaline conditions

Benjamin Cagnon, Stéphane Gin, Martiane Cabié, Damien Daval

▶ **To cite this version:**

Benjamin Cagnon, Stéphane Gin, Martiane Cabié, Damien Daval. International Simple Glass (ISG) dissolution rate in a (Si, Ca)-rich environment at 90 °C and alkaline conditions. Journal of Nuclear Materials, 2025, 603, pp.155426. 10.1016/j.jnucmat.2024.155426 . hal-04749359

HAL Id: hal-04749359

https://cnrs.hal.science/hal-04749359v1

Submitted on 23 Oct 2024

HAL is a multi-disciplinary open access archive for the deposit and dissemination of scientific research documents, whether they are published or not. The documents may come from teaching and research institutions in France or abroad, or from public or private research centers.

L'archive ouverte pluridisciplinaire **HAL**, est destinée au dépôt et à la diffusion de documents scientifiques de niveau recherche, publiés ou non, émanant des établissements d'enseignement et de recherche français ou étrangers, des laboratoires publics ou privés.

Distributed under a Creative Commons Attribution 4.0 International License

Journal of Nuclear Materials 603 (2025) 155426

Contents lists available at ScienceDirect

Journal of Nuclear Materials

journal homepage: www.elsevier.com/locate/jnucmat

International Simple Glass (ISG) dissolution rate in a (Si, Ca)-rich environment at 90 °C and alkaline conditions

Benjamin Cagnon [a], Stéphane Gin [b], Martiane Cabié [c], Damien Daval [a,*]

[a] Univ. Grenoble Alpes, Univ. Savoie Mont Blanc, CNRS, IRD, Univ. G. Eiffel, ISTerre, 38000 Grenoble, France
[b] CEA, DES, DPME, SEME, University of Montpellier, Marcoule, France
[c] Aix Marseille Univ, CNRS, Centrale Marseille, FSCM, CP2M, Marseille, France

ARTICLE INFO

Keywords:
ISG glass
Dissolution
Secondary phases
CSH
Basic pH

ABSTRACT

The dissolution of International Simple Glass (ISG) was investigated at 90 °C and alkaline conditions with various concentrations of dissolved Si and Ca to unravel the combined effects of those elements on ISG reactivity. Experiments were conducted over durations ranging from 20 days to 3 months. Through morphological, structural, and chemical characterizations, the glass dissolution rate was proven to be strongly correlated with the activity of dissolved silica in the solution. While dissolved calcium did not significantly impact the dissolution rate, precipitation of calcium silicate hydrates (CSH) during the experiments enhanced ISG dissolution rate, though to a modest extent. The 3-months experiments highlighted the strong correlation between the dissolution mechanism and the evolution of the nature of secondary phases in saturated solution. During the first 20 days and at high Si and Ca concentrations, CSH precipitated and aggregated, without preventing the passivating impact of the gel layer at the surface of the glass: the dissolution was controlled by diffusion. Then, a resumption of dissolution occurred between 19 days and 76 days, corresponding to the CSH growth, and a possible mechanistic switch to a hydrolysis-controlled reaction rate. Finally, in some experiments, a drop in pH due to carbonate precipitation was observed along with a decrease in the dissolution rate, falling back in a diffusion-limited regime. Overall, this study shows that at 90 °C, pH = 10 and concentrations of SiO_2(aq) exceeding 50 % of saturation with respect to amorphous silica, irrespective of Ca concentration but in presence of CO_2(aq), ISG exhibits a very good chemical durability.

1. Introduction

For decades, several countries have produced borosilicate glass to confine high level radioactive waste arising from reprocessing of spent nuclear fuel [1]. After cooling and interim storage, glass canisters will be disposed in a deep geological repository. The safety demonstration of such a disposal relies on a multi-barrier system in which glass is the primary barrier. Studying the long-term behavior of these materials represents a challenge for the scientific community as glass dissolution results from multiple processes which in turn depends on several intrinsic and environmental parameters [2-6]. One of the main scenarios of glass degradation involves a solution enriched in dissolved Si and Ca species, which alters the glass under alkaline conditions. To better understand basic mechanisms of glass dissolution, nuclear glass research community selected a six-oxide borosilicate glass called International Simple Glass (ISG) to provide a common benchmark material [7]. Many studies investigated the dissolution rate and dissolution mechanisms of this glass according to various parameters such as the pH, the temperature, silica concentration and calcium concentration, as well as the Si-Ca interaction forming secondary phases [4,5,8-15]. Some of the main findings are briefly recalled below.

The dissolution rate of ISG has been investigated by several studies as a function of pH and temperature [8,16,17]. The correlation between the initial dissolution rate and the pH was further evidenced by Inagaki et al., 2013[8] as the pH-rate relations observe a "V-shaped" curve with a minimum dissolution rate at pH 4 for temperatures ranging from 25 °C to 90 °C, and congruent dissolution in basic solutions. With several other studies [4,14,18], the authors supported a surface-reaction mechanism controlling the initial dissolution rate in a vast range of pH (1 – 10.7).

It must be recalled that, in general, a glass alteration layer is made of several sublayers which are (from the glass toward the solution): a hydrated alkali-depleted layer, a porous, amorphous and hydrated layer

* Corresponding author.
E-mail addresses: benjamin.cagnon@univ-grenoble-alpes.fr (B. Cagnon), damien.daval@univ-grenoble-alpes.fr (D. Daval).

https://doi.org/10.1016/j.jnucmat.2024.155426
Received 10 April 2024; Received in revised form 13 September 2024; Accepted 22 September 2024
Available online 25 September 2024
0022-3115/© 2024 The Author(s). Published by Elsevier B.V. This is an open access article under the CC BY license (http://creativecommons.org/licenses/by/4.0/).

also called gel, and an outer layer formed by precipitated phases, also called secondary phases. The thickness and the properties of these layers depend on various environmental parameters, such as the temperature, the pH or the solution composition. For instance, when ISG is altered in deionized water at 90 °C and at pH 7 or 9, no secondary phases forms [5,6]. The gel is passivating when it lowers glass dissolution rates. The physical reasons for that are the saturation with respect to amorphous silica in pore and bulk solutions, which reduces covalent bonds hydrolysis on the one hand, and the gel reorganization, which reduces the transport of reactants and products on the other hand. Focusing on ISG and the stability of alteration layers in silica saturated solution and deionized water, Fournier et al., 2019 [14] highlighted a negligible effect of the concentration of dissolved silica on the dissolution rate of ISG under acidic conditions, up to pH 7. At higher pH (around pH 9), the gel layer undergoes an *in-situ* reorganization, resulting in the decrease of the dissolution rate of the underlying glass [15]. However, this passivating layer becomes unstable when the pH increases, leading to the alteration resumption [14,15]. The presence of secondary phases at 90 °C and pH $>$ 10.1, such as calcium silicate hydrates (CSH) or zeolites neoformations, is also detrimental for the passivating properties of the gel [15,19] and can promote the hydrolysis of the silica network which becomes the driving force of the alteration resumption [15].

Regarding calcium, antagonist effects on glass dissolution rate were highlighted by several studies depending on the pH, the glass surface-area-to-solution-volume ratio (SA/V) and then the concentration of Ca [20-23]. Four different behaviors were proposed by Mercado-Depierre et al., 2013 [9]:

(i) at pH 7 – 8 and low SA/V ratio (25 – 50 m^{-1}), Ca formed metal complex on the surface of the material, increasing the initial dissolution rate of the glass.
(ii) at similar SA/V ratio but in basic pH conditions, Ca penetrated within the gel layer and due to Ca-Si reactivity, its transport properties decreased and thus, the initial dissolution rate was significantly reduced [20].

Those two cases (i) and (ii) correspond to scenarios where the low concentration of Si in solution prevented the precipitation of CSH and other Si-bearing secondary phases.

(i) at a high SA/V ratio (1 000 – 20 000 m^{-1}) and near neutral pH conditions, a Si-Ca rich passivating layer was suspected to form at the glass surface [9]. Furthermore, calcium also played a catalytic role in the densification of the gel layer, leading to the closure of porosity and ultimately, a decrease in the transport properties of the gel layer [10]. The presence of elements poorly soluble such as Al can impact the passivating properties of the gel [24-26].
(ii) at high SA/V ratio and basic pH, the solution is rapidly supersaturated with respect to CSH. As long as CSH precipitate, it was suggested that the glass dissolves at a rate close to the initial dissolution rate [21,27]. Conversely, Maraghechi (2016) [23] proposed that a protective layer formed by a dense, non-porous and strongly bounded CSH layer on the surface of the glass that could limit the glass dissolution rate.

It is widely known that the formation of secondary phases such as zeolites or CSH can significantly increase the dissolution rates of silicate glasses [9,28,29], especially in hyperalkaline pH [30]. However, some recent studies in which ISG was altered under alkaline conditions in young cement water reported the formation of secondary phases identified as zeolites and phyllosilicates, either without CSH [31], or with CSH having a low Ca/Si ratio [27] with no resumption of glass dissolution. This observation was related to the decrease in pH after some time of experiment [27]. The formation of CSH follows the general law of nucleation where the degree of supersaturation in solution controls the homogenous nucleation rate [32]. However, a more recent study demonstrated a two-steps CSH formation process. The first step consists in the formation of amorphous dispersed spheroids which are depleted in Ca compared to regular CSH (meaning a ratio of Ca/Si $<$ 0.6) and sodium plays the role of a charge compensator. After some time, the amorphous spheroids aggregate and sodium is exchanged with calcium, leading to the crystallization of the aggregates into a tobermorite-type CSH [33-35] (Ca/Si ratio close to 0.8). Other crystalline CSH phases have been under study over the years. Blanc et al., 2010 [36,37] summarized the thermodynamic properties of nanocrystalline and crystalline CSH phases with various structures.

In presence of carbon dioxide, CSH phases are metastable and are susceptible to carbonation. This process has been extensively investigated [38-44]. The Ca/Si ratio strongly influences the carbonation resistance of the CSH, but a consensus is yet to be reached on this issue. Some studies support that a lower Ca/Si ratio implied a higher carbonation resistance [45] while other studies support the opposite [39,44], i.e., CSH with a lower Ca/Si ratio tend to decompose faster in presence of carbonate. Due to their carbonation properties, some studies were carried out to investigate the sequestration of CO_2 using various calcium silicate hydrated phases [38,46,47]. The carbonation of CSH leads to mainly four carbonate by-products which are aragonite, vaterite, calcite and amorphous carbonate [41,48]. Following the CSH decomposition, a silica gel is formed. Liu et al., 2022 [38] demonstrated that the by-products of carbonation, their proportions and the carbonation rate is strongly related to the initial Ca/Si ratio in the CSH. On another note, they divided the carbonation process into 3 steps: a dissolution period where a progressive decrease of both Ca/Si and pH is observed with the formation of calcium carbonate, a diffusion period where small portions of CSH crosslink, leading to the formation of an amorphous phase they called “calcium modified silica gel”, and a reaction period where the CSH convert to calcium carbonates, with the amorphous phases remaining as a calcium-modified silica gel.

Of note, another impact of Ca had also been reported at various temperatures (from 30 °C to 90 °C), and at high pH (near pH 12.5), in presence of boron [12]. Initially, dissolved Ca precipitated with the boron leached from the borosilicate glass to form Ca $[B(OH)_4]_2$(s). To some extent, this first precipitate can prevent the glass dissolution by limiting the hydrolysis of the silicate matrix. However, when the solubility limit of CSH was reached, Ca $[B(OH)_4]_2$(s) became unstable and dissolved, releasing $B(OH)_4$- and Ca^{2+} into the solution. The calcium was then consumed to form increasing amounts of CSH, promoting the glass dissolution by trapping the silicon from the solution and from the glass [21,27]. In conclusion, the presence of B in the Ca-Si system resulted in an incubation period at the beginning of the glass dissolution process. This incubation period is shorter as the temperature increases (from 30 °C to 70 °C) and almost disappears at 90 °C.

Overall, the dissolution rate of borosilicate glass has been previously studied as a function of various parameters such as pH and temperature. The effect of dissolved Si and Ca species was also investigated separately from each other. The formation of CSH during the dissolution of silicate glass was observed but their effect on the dissolution rate remains debated. Furthermore, a proper understanding of the combined effect of dissolved Si and Ca species on the dissolution rate during the full process of CSH formation and carbonation is still lacking.

This study attempts to address these concerns, focusing on the evolution of ISG dissolution in Si- and/or Ca-rich solutions at 90 °C and pH =10 (except when mentioned, all pHs below are given at 90 °C). The effect of CSH neoformation on the ISG dissolution rate and insights on the CSH formation kinetics during 20-day and 3-month experiments are reported. Overall, these results suggest that although the formation of CSH triggers a significant resumption of ISG dissolution, this effect is rapidly counterbalanced by the carbonation of CSH, so that under the investigated conditions, ISG exhibits very good chemical durability.

2. Materials and methods

2.1. Overall presentation

Various series of experiments were conducted at 90 °C to unfold the relation between the concentration of Si and Ca in solution and the alteration of ISG samples in alkaline conditions. Si and Ca are expected to interact and potentially form CSH. The composition domain that we investigated was delimited by the solubility of amorphous silica (SiO_2(am)) for the Si endmember, and portlandite ($Ca(OH)_2$) for the Ca endmember. Using the thermodynamic code JChess [49] and the Thermochimie database provided by Andra [36,37,50-53] (https://www.thermochimie-tdb.com/), the domain of stability of CSH was calculated with 3 different Ca/Si ratios that are provided in the database (CSH0.8, CSH1.2 and CSH1.6, where each number refers to the Ca/Si ratio in the structure of the CSH). Those solubility lines are displayed in Fig. 3 to evidence their domain of stability in the activity diagram.

The saturation state of the solution with respect to amorphous silica corresponds to a theoretical concentration of dissolved Si of 8.75×10^{-2} mol.L^{-1} at pH = 10. The activity of H_4SiO_4(aq) in these conditions corresponds to 0.0052 molal, which determines the solubility limit of $SiO_{2(am)}$ in the activity diagram (see Fig. 3), i.e., $\log(a(SiO_2)) = -2.286$. Regarding calcium, the saturation with respect to portlandite corresponds to 1.5×10^{-1} mol.L^{-1} at pH 10. The equilibrium activity of Ca^{2+} (0.034 molal) and the activity of H^{++} (8.00×10^{-11} molal) provide the solubility limit of portlandite under such conditions, i.e., $\log(a(Ca^{2+})/a(H^+)^2) = 18.73$.

The domain of precipitation of CSH is clearly defined and several experiments were conducted to investigate the reactivity of ISG in this thermodynamic field. The name and initial conditions of each series of experiments are described in Table 1.

As the experiments were conducted under static conditions, a shift in pH and solution composition was expected, as the solution was not restricted precisely to a specific, well-defined condition. Flow-through experiments would have had the ability to circumvent this issue. However, the likely precipitation of secondary phases in tubings prevented us from conducting the experiments in flow-through set-ups. In case of experiments conducted near the saturation state with respect to amorphous silica, the high level of dissolved Si species contributed to buffer the solution since H_4SiO_4 is a weak acid.

2.2. Experiment preparation

The ISG used in this study is referred to as ISG-1 (wt% 56.2 SiO_2, 17.3 B_2O_3, 12.2 Na_2O, 6.1 Al_2O_3, 5.0 CaO, 3.3 ZrO_2) and its elaboration conditions are detailed in Ryan et al., 2022 [54]. Glass coupons with dimensions of $2 \times 2 \times 0.1$ cm^3 originated from CEA Marcoule, France, were polished by PrimeVerre, France, following their 6 faces with a 1/4 μm diamond grain paste at the last step. Once polished, ISG coupons were cut into smaller pieces using a diamond saw. Except for series A, E and H, a small part (<1 mm^2, on average <5 % of the polished surface) of the top and bottom surfaces of ISG samples was protected with room-temperature-vulcanizing (RTV) glue spots to create a non-reacted reference surface used for subsequent topography analyses run with vertical scanning interferometry (VSI, see below). For the series D, F and J, the entire ISG glass coupon was used for the experiment, and 4 small parts of the top and bottom surfaces were protected with RTV glue. Once the experiment was over, the coupon was cut into smaller pieces using a diamond saw in dry conditions in order to prevent further degradation of the materials after the experiment due to the presence of a solvent.

The experiments were conducted in solutions with various concentrations of Si and Ca (see Table 1), and the series were named following increasing SiO_2(aq) concentrations (Ai to Hi, with i a number ranging from 0 to 4 to account for the initial Ca concentration in the

Table 1
Summary of the initial conditions for all series run in the present study. The first column refers to the name of the experiments, which were sorted out according to the initial Si concentration in the fluid (except for series J, which corresponds to experiments all run over longer durations, but at various high Si concentrations). The second and third columns refer to the initial SiO_2(aq)/SiO_2(aq)$_{eq}$ ratio and the initial concentration of Ca (ppm) in the solution. The fourth and fifth columns refer to the logarithm of the activity of SiO_2(aq) and that of the $Ca^{2+}/(H^+)^2$ activity ratio. The sixth column refers to the duration of the experiment at the time of collection. The seventh, eighth and ninth columns refer to the difference in Gibbs free energy related to the dissolution of CSH0.8, CSH1.2 and CSH1.6 respectively based on JChess calculations. Note that the concentration of Ca reported with (*) are the theoretical values based on weighing, as the ICP-OES analyses failed for the corresponding samples.

Series	Si/Si$_{eq}$	[Ca] (ppm)	log(a(SiO_2))	Log [a(Ca^{2+})/ a(H^+)^2]	Time (days)	ΔG(CSH0.8) (J.mol^{-1})	ΔG(CSH1.2) (J.mol^{-1})	ΔG(CSH1.6) (J.mol^{-1})
A1	0 %	280.30	−5.07	17.45	18.0	−2140	−2494	−3543
A2	0 %	276.90	−5.04	17.45	18.0	−2044	−2395	−3441
A3	1 %	264.20	−4.55	17.42	18.0	−640	−1029	−2112
B1	0 %	9.10	−4.86	16.08	17.0	−4813	−6822	−9525
B2	0 %	60*	−4.87	16.60	17.0	−3603	−4987	−7065
B3	0 %	380*	−4.88	16.46	17.0	−3947	−5498	−7744
B4	0 %	780*	−4.88	16.76	17.0	−3258	−4452	−6340
C1	2 %	5.30	−4.03	15.88	17.1	−2783	−5031	−7974
C2	2 %	44.90	−4.06	16.75	17.1	−787	−1993	−3894
D1	9 %	1.64	−3.26	15.48	21.0	−1454	−4193	−7628
D2	18 %	0.03	−2.97	13.72	21.0	−4827	−9691	−15,253
E1	44 %	0.01	−2.82	13.17	15.1	−5682	−11,212	−17,436
F1	49 %	639.76	−2.61	17.84	23.8	6227	6344	5766
G0	35 %	2.50	−2.69	13.96	21.0	−3402	−7976	−13,245
G1	54 %	1.72	−2.52	15.13	21.0	−64	−3226	−7082
G2	55 %	73.91	−2.51	16.75	21.0	3903	2703	807
G3	57 %	117.26	−2.51	16.93	21.0	4338	3355	1677
G4	56 %	280*	−2.52	16.45	21.0	3139	1569	−695
H1	79 %	1.00	−2.46	14.89	14.0	−448	−3902	−8050
I1	84 %	7.00	−2.35	15.86	19.0	2227	−51	−3024
I2	86 %	55.56	−2.35	16.75	19.0	4400	3204	1313
I3	86 %	299.48	−2.36	17.46	101.0	6078	5737	4702
I4	100 %	761.89	−2.32	17.83	101.0	7079	7178	6583.5
J2	44 %	149.73	−2.62	17.26	101.0	4781	4190.8	2905
J3	97 %	449.10	−2.32	17.62	101.0	6567	6411	5560
J4	82 %	764.95	−2.40	17.85	101.0	6890	7022	6459
J4bis	103 %	894.25	−2.31	17.89	101.0	7242	7415	6894

corresponding series). The J series corresponds to experiments run over longer durations and elevated concentrations of SiO_2(aq).

A stock solution saturated with respect to amorphous silica (SiO_2(am)) was prepared using nanopowder silica (specific surface area 175 – 225 $m^2.g^{-1}$, 99.8 % trace metals basis). The pH was measured at high temperature (90 °C) and adjusted to 10.1 ± 0.1 by addition of LiOH (Prolabo) on a daily basis. After the solution pH stabilized (approximately 10 days), the CO_2 in the solution was removed by degassing with N_2 (0.15 $L.min^{-1}$) at high temperature (near water ebullition, $T > 90$ °C) during 30 min for 500 ml of solution. The presence of dissolved CO_2 in the solution favors the precipitation of calcium carbonate, preventing possible reaction between calcium and dissolved silica. PFA Savillex® vessels, containing a PTFE tripod for the experiments carried out first (series E, H) or a Teflon basket (the remaining series), were filled with approximately 50 mL of solution and placed in a N_2 atmosphere-controlled glove box. The appropriate amount of Ca was added to each reactor by sampling aliquots from a stock solution prepared with dissolved $CaCl_2$. Only 1 mL or 2 mL of solution containing Ca was added. The addition of calcium during experiments E2 to E4 revealed an instantaneous precipitation of secondary phases. A lack of control on the chemical evolution of the solution was noticed based on sample collection, before the solution reached an apparent steady-state composition. As a consequence, (i) the experiments E2 to E4 were discarded from the present dataset, and (ii) for all subsequent experiments conducted in the stability domain of CSH (series F to J), after the addition of calcium, each reactor was placed in an oven at 90 °C for an incubation time of 24 h. The initial sample was collected right before the addition of the ISG coupon. Each reactor was then placed in an oven at 90 °C and the solutions were continuously stirred with magnetic bars. Note that no specific protocol was followed to limit any ingress of CO_2 into the reactors while stored in the oven, which becomes noticeable for experiments typically exceeding 3 weeks under our conditions. The collected samples were filtered using a 0.45 µm pore size filter before dilution. For the series F, I and J, the collected samples were diluted with a factor x5, x150 and x1500 using ultrapure water (18.2 MΩ.cm) and the supernatant from the solution diluted 5x was collected with a micropipette before analysis.

After introducing the coupons in the reactors containing the prepared solution, the dissolution of the glass started in the oven at 90 °C (see Fig. 1). After an intermediate timestep of 7 to 10 days, each reactor was placed in the glove box in order to collect a second sample. At the end of the experiment, every reactor was placed in the glove box to recover both the solution and the ISG coupon.

After alteration, the ISG coupons were dipped three seconds in ultrapure water before being immersed for three seconds in ethanol. They were dried and stored in the glove box at room temperature until surface analyses were conducted. After the last sampling collection of the solution, the remaining precipitates were collected with two centrifugation steps: the aim of the first one was to concentrate the solid to remove the solution and the aim of the second one, conducted in ethanol, was to remove the remaining water to ease the collection of precipitates. They were then stored in the glove box prior to Infra-Red (IR) spectroscopy analyses and Scanning Electron Microscopy (SEM) observations coupled with Energy Dispersive X-Ray Analysis (EDX).

2.3. Fluid and solid analyses

2.3.1. ICP-OES analyses of aqueous solution

The dissolution process was monitored by collecting 2 mL of the solution at the beginning of the experiment, after 7 to 10 days of reaction and at the end of the experiment. The samples were then diluted 5x, 150x and 1500x and analyzed with Inductively Coupled Plasma Optical Emission Spectrometer (ICP-OES) (Varian 720-ES) for Na, B, Al, Si and Ca. At each sampling duration, the concentration of Si and Ca was measured in the solution in order to account for the saturation state of the solution. The concentrations were implemented in JChess [49] to calculate the activity of those two elements and then position the chemical status of the solution in the activity diagram shown in Fig. 3.

The measured concentrations of B and Na were used to calculate the location of the 'internal interface' (interface between the gel layer and the pristine (non-reacted) glass) and the glass dissolution rate (see Wild et al., 2016 [13] for details). This dissolution rate may correspond to the growth rate of the gel layer if the external interface of the layer is stable (i.e., if it does not dissolve, as can be expected when the solution is saturated with respect to SiO_2(am)).

The equivalent thickness, $Eth(i)$ (mm), of altered glass was calculated based on ICP-OES measurements of the amount of B and Na released into the fluid, following:

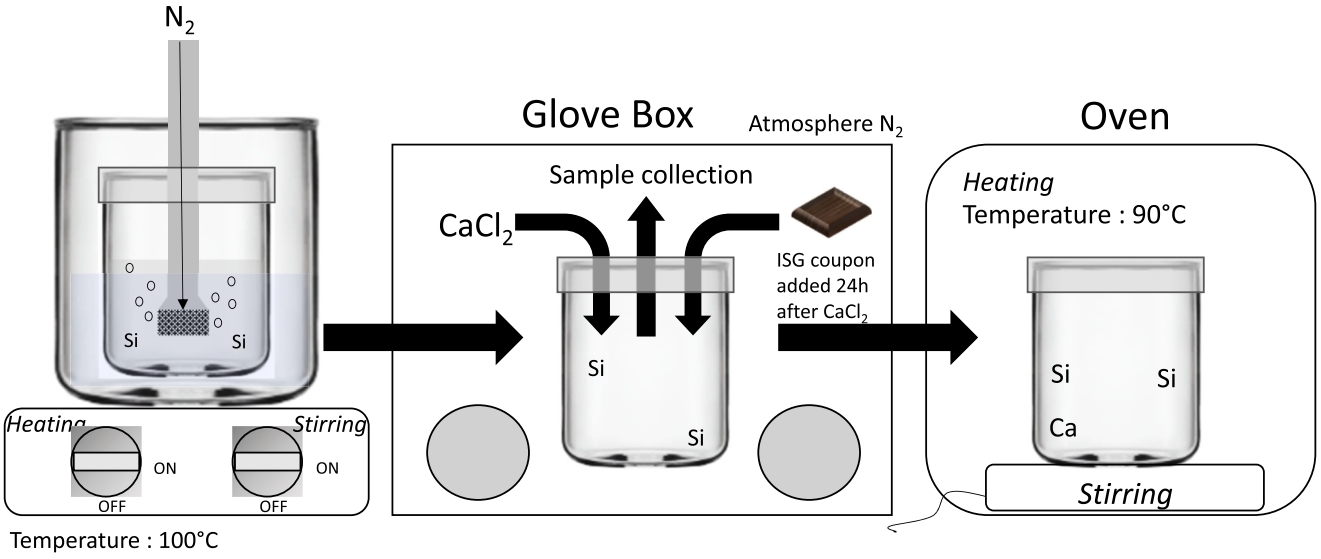

Fig. 1. Schematic representation of the various steps of experiment preparation. After degassing the 500 mL Si-rich solution with N_2 during 30 min, the reactor was placed in the glove box where Ca was added in the form of $CaCl_2$ from a concentrated solution. The reactor was placed in an oven heated at 90 °C for 24 h and then put back in the glove box for sample collection and the addition of the ISG coupon. Finally, the reactor was placed back in the oven, which represented the onset of the dissolution experiments.

$$Eth(i) = \frac{[i]_t \times F_t \times V_t}{SA \times \rho \times x(i)} \quad (1)$$

where $[i]_t$ is the concentrations (ppm) of element i (B or Na) at time t measured by ICP-OES, F_t is the dilution factor of the aqueous sample collected at time t, V_t is the volume (L) of the solution in the reactor just before collection (the correction on the volume due to the sampling was negligible compared to the uncertainties of the ICP and therefore omitted in the calculation), SA is the sample surface area (mm^2), ρ is the specific volume of ISG glass ($\rho = 2.498$ $mg.mm^{-3}$) and $x(i)$ is the mass proportion of the element i in ISG ($x(i) = 0.0905$ for Na in ISG and $x(i) = 0.0537$ for B in ISG). Eth(i) is equal to the gel layer thickness when the alteration is isovolumetric (see Fig. 2).

Based on the equivalent thickness calculated at two different stages, the corresponding dissolution rates were calculated following:

$$r_{disso}(i) = \frac{\Delta Eth(i) \times \rho}{\Delta t} \quad (2)$$

where $r_{disso}(i)$ is the dissolution rate ($g.m^{-2}.d^{-1}$) calculated based on the release of the element i, $\Delta Eth(i)$ is the difference between two consecutive equivalent thicknesses based on the element i, and Δt is the time interval between two consecutive samples.

Overall, the dissolution rate calculated based on the release of B in solution ($r_{disso}(B)$) was in good agreement with the dissolution rate calculated based on the release of Na in solution ($r_{disso}(Na)$). They were linearly correlated with a correlation coefficient $R^2 = 0.92$ (see Supplementary Fig. S1). However, $r_{disso}(Na)$ was systematically lower than $r_{disso}(B)$, shifting the linear regression to a slope with a value of 1.3. Furthermore, the Na and B analyzed concentrations are low (ppb to ppm) and Na is an element that is more sensitive to contamination than B. As shown below, $r_{disso}(B)$ was found to be in better agreement with the dissolution rate calculated based on the solid characterization (see Fig. 4 and Supplementary Fig. S2), so that in the following, $r_{disso}(B)$ was considered to better reflect ISG reactivity, and $r_{disso}(Na)$ was not considered in the subsequent analyses.

2.3.2. VSI, IR and SEM-EDX analysis of the sample

The retreat of the glass resulting from dissolution was measured using RTV glue masks to create a non-reactive reference surface. Topography analyses were then conducted using VSI (Zygo Newview 7300) (Figs. 5 and 6). For all samples, the images were taken at 10x-magnification, corresponding to a lateral resolution of 1.7 μm, while the vertical resolution was on the order of 1 nm. Supplementary Table S1 provides information on the surface retreats measured on coupons by VSI.

SEM observations were conducted with a Tescan Vega 3 operated at ISTerre (Grenoble, France). SEM analyses were performed on each sample which was gold-coated (1 nm) beforehand. Energy Dispersive X-ray (EDX) spectra were acquired with an SDD detector from Rayspec to probe the chemical composition of both the surface of each reacted coupon and the precipitates formed in the solution or on the surface. The used incident energy was 16 keV.

Finally, infrared (IR) analyses were performed using a Thermoscientific infrared analyses instrument in Attenuation Total Reflectance (ATR) mode to probe the surface of the altered sample. Before analysis, ISG samples were cleaned with ethanol and air-dried. A background analysis was conducted before each measurement. The thickness of the analyzed surface was up to 1 μm. In the present study, the direct use of IR often proved challenging to directly detect the presence of CSH because the vibration modes characteristic of CSH structures (980 cm^{-1} to 920 cm^{-1}, according to their Ca/Si ratio) overlap with those of amorphous silica (see Supplementary Fig. S3). The IR analyses were then coupled with SEM-EDX and thermodynamic modeling to infer indirectly the presence of CSH, i.e., CSH precipitation was suspected when the characterizations observed the three following conditions: i) The solution is close to saturation or supersaturated with respect to CSH, ii) SEM-EDX analyses of the reacted ISG coupon reveal a Ca/Si ratio higher than on a pristine ISG coupon and the observed morphology typical of CSH and iii) IR analyses do not reveal peaks related to calcium carbonates, which are the main phases with which CSH compete for Ca consumption.

2.3.3. ToF-SIMS analyses of the sample

The altered solid samples were analyzed by an IONTOF GmbH® TOF 5 spectrometer from TESCAN Analytics (France). The external surface was abraded on an area of 200 × 200 μm^2 for an analyzed area of 50 × 50 μm^2. The ToF-SIMS operated as cycles of abrasion and analysis. After each cycle, the surface charge was neutralized by a low energy electron beam (< 20 eV) in order to prepare the area for the next cycle. The depth of the crater (h_{crater}) created by ion milling after a given number of abrasion cycles (N_{cycles}) was measured using 3D profilometer. The depth associated to one cycle of abrasion (z_{cycle}) is then assumed to be simply given by:

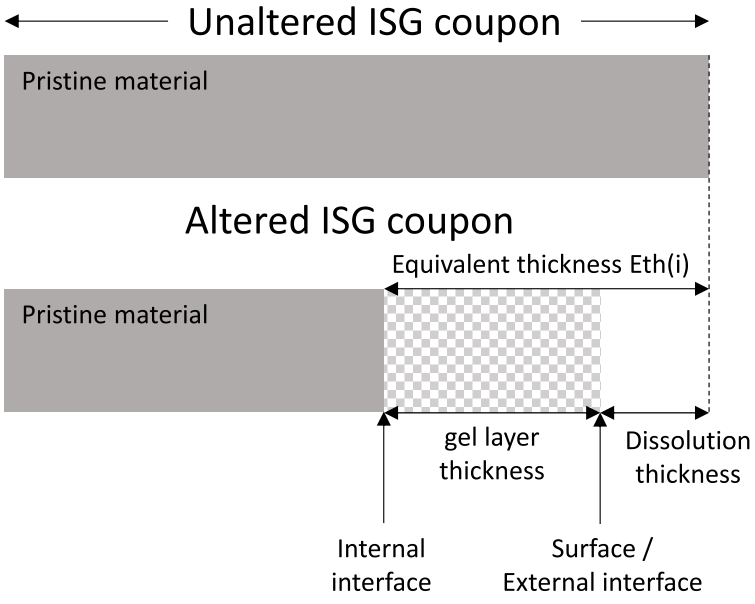

Fig. 2. Schematic representation of the interfaces and terminology used in this study.

$$z_{cycle} = h_{crater}/N_{cycles} \quad (3)$$

Uncertainties are approximately 15 % of the result value of h_{crater}. Depth profiles of positive ions, O^+, Na^+, Al^+, $^{28}Si^+$ and $^{29}Si^+$ were recorded thanks to Bi_1^+ 25 keV, 1.2 pA beam for the analyses and O_2^+ 2 keV, 600 nA beams for the ablation. Only information related to the thickness of the gel layer, analyzed by ToF-SIMS, are reported in this study (see Supplementary Table S1). The detailed profiles will be provided in an upcoming study.

2.3.4. FIB-TEM analyses of the sample

The reacted samples were platinum-coated at TESCAN Analytics (France), and ultrathin electron transparent cross sections were subsequently prepared by focused ion beam (FIB) milling following methods previously described by Daval et al., 2009 [55] and summarized in Cagnon et al., 2022 [24]. FIB foils were then analyzed using transmission electron microscopy (TEM) and scanning transmission electron microscopy (STEM) using a FEI Tecnaï G2 microscope with a LaB6 electron source operating at 200 kV, operated at CP2M (Marseille, France). EDX spectra were acquired in STEM mode to probe the chemical composition of the interface between the gel layer and the substrate, with an Energy Dispersive X-ray Detector (Oxford XMax 80). The analysis was conducted on some substrates (see Supplementary Table S1).

3. Results

In this section, the dissolution rates calculated using solution analyses are presented first, before being compared to the dissolution rates calculated from solid characterizations. As precipitates were observed in the solution, their effects on the dissolution rates are discussed. To reach this goal, the nature of those precipitates was studied before attempting to establish a link between those phases and glass dissolution rate. Finally, long-duration experiments (101 days) were investigated through the chemical composition of the solution and their precipitates.

3.1. Dissolution rates calculated using solution analyses

Fig. 3a shows an activity diagram plotted using the solution data coming from the different series conducted in the present study. Additional data on ISG alteration from Fournier et al. (2019) [14], which were collected in a solution with no initial addition of Ca in the solution, were also reported to the figure. The subset of data that we selected from their study observed the following conditions: i) no zeolite or other secondary phase precipitated in the solution; ii) The initial pH was not significantly lower than the pH at which the experiments of this study were conducted (i.e., 10 ± 0.2 after 20 days of alteration). This second condition ruled out all the experiments from Fournier et al. (2019) [14] conducted at pH ≤ 9.5. According to the above-mentioned criteria, only three sets of experiments were selected for comparison: S1-Blk-10.1, S2-Blk-9.8 and S2-Sat-9.8. ISG dissolution rates calculated from B release were then reported in Fig. 3b.

From the activity diagram where the saturation lines with respect to 3 different CSH are displayed, two domains can be defined: the one where the solution is undersaturated with respect to all of the 3 CSH, and another one where the solution is saturated with respect to any of the 3 CSH. Most rate data from Fournier et al. (2019) [14] fall in the undersaturated domain (open circles in Fig. 3a), at least with respect to CSH1.2. Most rate data collected in the present study are situated in the stability field of the 3 CSH compositions mentioned previously. Of note, the evolution of the chemical composition of the solution from series B followed the saturation line of the CSH0.8 (Fig. 3a). Therefore, the solutions were assumed to remain in equilibrium with the selected CSH0.8 throughout the experiment, which was confirmed by IR and SEM characterizations (see Section 2 in Discussion), while no carbonate was found in this series.

The dissolution rates of ISG are reported in Fig. 3b. The main observation is that the dissolution rate decreases with increasing SiO_2(aq) up to near saturation conditions with respect to amorphous silica. The highest dissolution rate is observed with the lowest concentration of silica in the solution, i.e. log(SiO_2(aq)) = −5.16 and −4.88. No significant differences were observed at this stage in the dissolution rate between experiments where CSH precipitated and where they did not. However, when experiments near saturation with respect to amorphous silica are compared with S2-Blk-9.8 (located in the red square reported in Fig. 3) from Fournier et al., 2019 [14], a discrepancy is observed. The rates calculated from this latter specific experiment, with a log (SiO_2(aq)) between −3.5 and −3, appear as blue circles in Fig. 3b, meaning that they are lower than those from other experiments from the series F, G, I, and J that have a higher silica concentration, and which were all conducted in the CSH saturation domain.

3.2. Dissolution rates calculated using solid and solution analyses

As mentioned above, glass dissolution rates were estimated using different methods, i.e., ICP-OES, which was used to monitor the release of B in the solution, and a combination of VSI to measure the surface

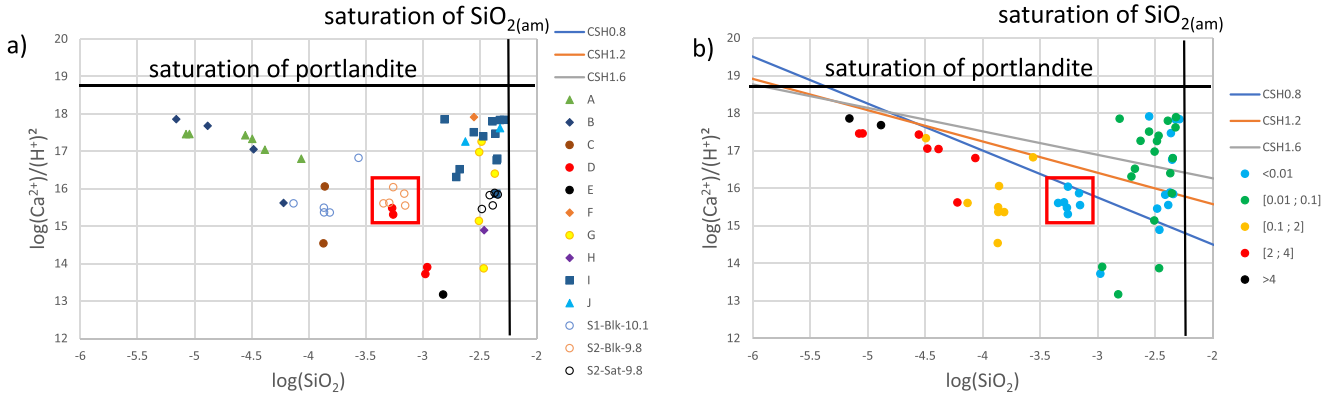

Fig. 3. Activity diagrams for the system CaO-SiO_2—H_2O representing the chemical composition of the solution of each reactor at the moment of the aqueous sample collection. The blue, orange and grey lines represent the saturation lines of CSH0.8, CSH1.2 and CSH1.6 respectively. The black horizontal line corresponds to the saturation line with respect to portlandite and the black vertical line corresponds to the saturation line with respect to amorphous silica. In the plot a), the filled symbols correspond to experiments carried out during this study while the open circles correspond to experiments carried out in Fournier et al., 2019 [14]. In the plot b), the same data were represented, but each color corresponds to a range of glass dissolution rates (in $g.m^{-2}.d^{-1}$) with the color code corresponding to increasing rates from blue to black. The data points located in the red square correspond to S2-Blk-9.8 experiment from Fournier et al., 2019 [14], and aims to highlight the discrepancy with the series F, G, I and J. (For interpretation of the references to colour in this figure legend, the reader is referred to the web version of this article.)

retreat, and ToF-SIMS and FIB-TEM to determine the gel layer thickness. Dissolution rates based on solid characterizations (*r_solid*) are in reasonable agreement with those calculated from elemental release (see Supplementary Table S2 and Supplementary Fig. S2). Overall, the dissolution rate decreases with the increase in $[SiO_2(aq)]/ [SiO_2(aq)]_{eq}$ ratio regardless of the method of calculation, which is consistent with the observations reported in Fig. 3. Note that the $[SiO_2(aq)]/ [SiO_2(aq)]_{eq}$ ratio is the distance to the saturation state of the solution with respect to amorphous silica.

From Fig. 4, two groups of dissolution rates are observed. The first one corresponds to a high dissolution rate with a low $[SiO_2(aq)]/ [SiO_2(aq)]_{eq}$ that ranges from 0 % to 2 %. The calculated dissolution rate is greater than 1 $g.m^{-2}.d^{-1}$ without exceeding 10 $g.m^{-2}.d^{-1}$ and both $r_{disso}(B)$ and r_{solid} are equivalent, within experimental uncertainties. The second group corresponds to lower dissolution rates, for $[SiO_2(aq)]/ [SiO_2(aq)]_{eq}$ greater than 9 %. Here, the dissolution rates range from 0.1 $g.m^{-2}.d^{-1}$ to 0.001 $g.m^{-2}.d^{-1}$ for $[SiO_2(aq)]/ [SiO_2(aq)]_{eq}$ ranging between 9 % and 100 %.

3.3. Characterization of the precipitates

Typical characterizations of the run products collected at the end of experiments are reported in Figs. 5 and 6. The characterizations were reported according to the two domains previously mentioned, with either a low (Fig. 5) or a high (Fig. 6) $[SiO_2(aq)]/ [SiO_2(aq)]_{eq}$ ratio. IR analyses were also reported and were used, coupled with SEM-EDX to determine the presence of CSH (see "Material and Methods" for more details).

3.3.1. Experiments run with a low $[SiO_2(aq)]/ [SiO_2(aq)]_{eq}$ ratio

Regarding the experiments conducted with a low $[SiO_2(aq)]/ [SiO_2(aq)]_{eq}$ ratio, the series A were run with a high initial concentration of Ca (> 260 ppm). The initial concentration of Si increased from A1 to A3. While the initial amount of aqueous silica remains low (from 0 to 1 % of saturation with respect to amorphous silica, see Table 1), the amount of precipitates in the solution and their morphology were different. Almost no precipitate was observed in A1, a small amount of gel-like material was observed in A2, and a larger amount of precipitates was observed in A3 (Fig. 5a). The A3 coupon surface remained neat and the precipitates in the solution were thin and presented a layer-like morphology. As it can be seen in Fig. 5a, they aggregated to form bigger precipitates with an average Ca/Si ratio around 0.6. IR analyses provided insight on the potential presence of CSH with a Ca/Si ratio of 0.7 for A3, which is consistent with the SEM-EDX analyses and with the fluid composition, which follows the saturation limit of CSH0.8 (Fig. 3). Those observations strongly suggested the presence of CSH in the A3 experiments' precipitates.

The series B and C were also carried out with no or little Si added (between 0 % and 2 % of SiO_2(am) saturation). The amount of calcium initially introduced increased from C1 to C2 and from B1 to B4. Precipitates were observed in both C1 and C2 and were also observed from B1 to B4. The average value of the Ca/Si ratios of the precipitates was around 0.6 for B3 (Fig. 5b) and ranged between 0.25 and 0.32 for C1 (Fig. 5c). The VSI analyses highlighted a step at the edge of the locations where the RTV glue mask was, which results from the dissolution of the glass (Fig. 5c). The step height was 13.6 µm for C1 and around 33 µm for B3, which compares favorably with the alteration thicknesses of 12.4 µm for C1 and 34 µm for B3 calculated from ICP-OES data. Note that B3 and A3 possessed a similar solution composition. The IR analyses are presented in Fig. 5d for the series B. Except for B4 and C2, no calcium carbonate peak was found for B1, B2 and B3 and C1 . However, peaks related to CSH were found and presented a local maximum between 980 cm^{-1} and 920 cm^{-1}. Based on Zhakiyeva (2021) [56] work, these maxima correspond to a standard CSH with a Ca/Si ratio close to 0.66 for B3, and 1.26 for C1, respectively, strongly suggesting the presence of CSH in the solution.

3.3.2. Experiments run with a high $[SiO_2(aq)]/ [SiO_2(aq)]_{eq}$ ratio

Strikingly, the apparent solubility of the gel layer seemed to be reached for a $[SiO_2(aq)]/ [SiO_2(aq)]_{eq}$ as low as 9 % (series D): the surface retreat is below 20 nm, while the thickness of the gel is around 40 nm. Experiments E1 and H1 are representative of series where no calcium was added in the solution, but with high $[SiO_2(aq)]$ concentrations, (i.e. $[SiO_2(aq)]/ [SiO_2(aq)]_{eq} = 44$ % for E1; and 79 % for H1). Fig. 6b is a typical SEM image representative of the corresponding coupons reacted in conditions close to the saturation with respect to amorphous silica and a low concentration of Ca (a few tens of ppm). The precipitates were essentially made up of a Si-rich gel-like surface coating. The TEM characterizations revealed that the gel layer thickness was 243 nm. H1 precipitates are shown in Fig. 6f. The amount of aqueous silica was higher compared to E1, and the gel layer thickness was thinner, about 50 nm, as inferred from TEM analyses.

Finally, the series G was carried out with a solution close to saturation with respect to amorphous silica, and an increasing amount of calcium from G0 to G4. Note that for both G3 (Fig. 6c) and G4 (Fig. 6d), Ca was introduced in the solution in the form of $^{44}CaCO_3$, instead of

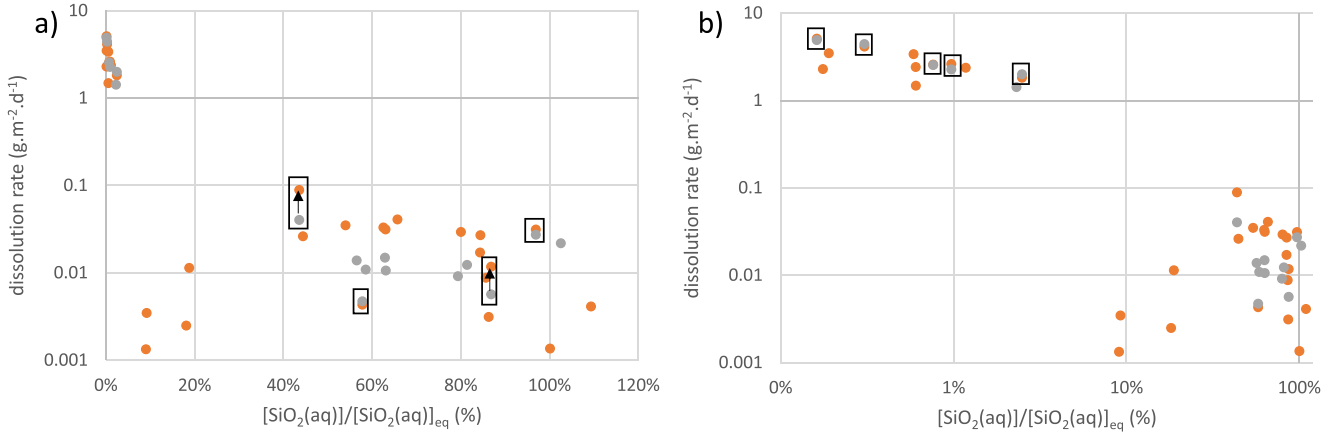

Fig. 4. Dissolution rate of ISG ($g.m^{-2}.d^{-1}$) as a function of the $[SiO_2(aq)]/ [SiO_2(aq)]_{eq}$ ratio (%). Both plots represent the same data. The orange circles represent the dissolution rates calculated based on the release of B in the solution determined by ICP-OES, while the grey circles represent the dissolution rates calculated based on solid analyses (VSI + ToF-SIMS or FIB-TEM). The conditions for which the rate calculation was performed for a same experiment based both on the solution and the solid analyses are highlighted in rectangles. (a) Semi-log plot of the relation between aqueous Si concentration and rate data, highlighting experiments conducted in Si-rich solutions. (b) Log-log plot of the relation between aqueous Si concentration and rate data, highlighting experiments conducted in Si-low solutions. (For interpretation of the references to colour in this figure legend, the reader is referred to the web version of this article.)

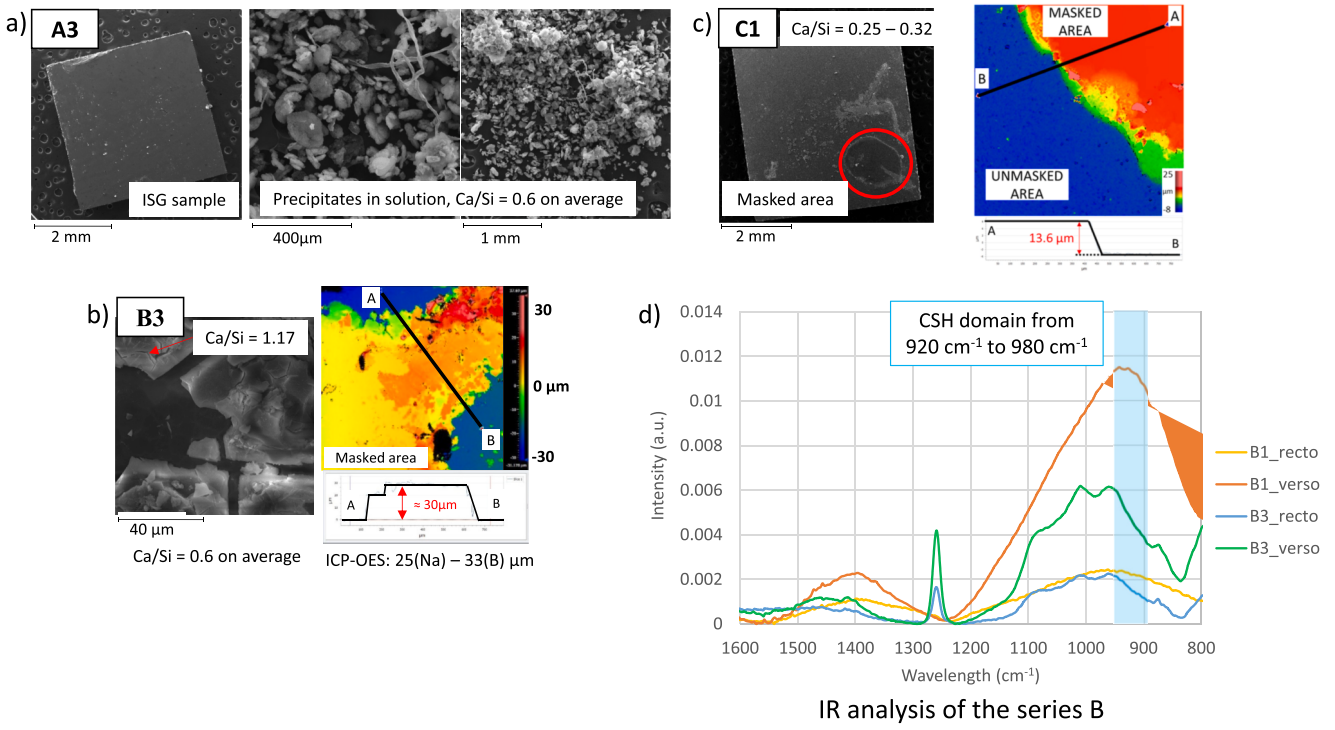

Fig. 5. Representative SEM, EDX and VSI characterizations of solids recovered from various experiments with a low $[SiO_2(aq)]/ [SiO_2(aq)]_{eq}$ after 20 days at pH 10 and 90 °C. a) SEM pictures of A3 surface coupon and precipitates in solution. b) SEM picture of B3 surface sample. The EDX spectrum revealed the presence of C on the area where the Ca/Si value is 1.17. A VSI analysis of the masked area after removal of the mask is also shown. c) SEM picture and VSI analysis of C1 surface sample. d) IR analysis on the series B. The yellow, orange, blue and green lines correspond to B1_recto, B1_verso, B3_recto and B3_verso faces, respectively. The recto (up-facing) and verso (down-facing) mentions were used to distinguish between the faces facing upwards or downwards. No difference between the face was expected as the solution was stirred and the sample was placed in a basket. The blue area is the domain where the peak of CSH with a Ca/Si ratio from 0.66 to 1.46 is expected. See Supplementary Note 3 for detailed band assignments to vibrational modes in this wavelength range. (For interpretation of the references to colour in this figure legend, the reader is referred to the web version of this article.)

$CaCl_2$, to trace the incorporation of Ca in secondary phases (the corresponding results will be discussed in an upcoming study). On the surface of ISG coupon, the average Ca/Si ratio was between 0.2 – 0.3 for G2, 0.45 for G3 and 0.60 for G4. The precipitates of both latest experiments are mainly calcium carbonates with a morphology of either cauliflowers or elongated crystals that may correspond to vaterite and aragonite, respectively. The first one was present in large amount whereas the second one was present as a minor phase. The EDX analyses confirmed an enrichment in Ca in those precipitates with a Ca/Si ratio between 2.0 and 2.6. Regarding G2, amorphous silica was among the main precipitates and, in some locations, EDX analysis confirmed a Ca/Si ratio of 1.88. The IR analyses of the series G are presented in Fig. 6e. Peaks related to calcium carbonates were only observed in the G3 and G4 precipitates, as well as on the surface of G3 and G4 coupons. No local maximum related to CSH precipitate could be isolated in the range of wavenumbers characteristic of these phases, except for G2, where peaks corresponded to CSH with a Ca/Si ratio of 1.6. Those observations suggested that out of the 5 series G experiments, CSH only precipitated in G2 experiment.

Of note, the VSI images shown in Fig. 6a are representative of the VSI analyses made on every experiment with a $[SiO_2(aq)]/ [SiO_2(aq)]_{eq}$ exceeding 9 %, including the series G. Little to no retreat was observed between the masked and unmasked areas of coupons reacted in those series.

3.4. Dissolution rate comparison according to the presence of CSH

Regarding the $[SiO_2(aq)]/ [SiO_2(aq)]_{eq}$ ratio from 0 % to 2 % (Fig. 7b), the experiment with CSH corresponds to A3 while the open yellow circles correspond to the series B. All experiments in this domain lasted around 20 days and regardless of the presence of CSH, the dissolution rate varies within the same order of magnitude. When the rate data obtained in the present study are combined with those collected by Fournier et al. (2019) [14], a continuous decreasing trend from $[SiO_2(aq)]/ [SiO_2(aq)]_{eq}$ ≈2 % to ≈15 % is evidenced. Around this latter $[SiO_2(aq)]/ [SiO_2(aq)]_{eq}$ ratio, the dissolution rate ranges from 7×10^{-4} to 4×10^{-3} $g.m^{-2}.d^{-1}$, which is of a same order of magnitude as the dissolution rate of experiments carried out at $[SiO_2(aq)]/ [SiO_2(aq)]_{eq} >$ 9 % in our study. Thus, a discontinuity between both domains is observed.

According to our results, at $[SiO_2(aq)]/ [SiO_2(aq)]_{eq} >$ 44 %, the dissolution rate varies from 1.4×10^{-3} to 8.8×10^{-2} $g.m^{-2}.d^{-1}$. The rate data from Fournier et al. (2019) [14] lies in the lower part of this range, between 2.0×10^{-3} and 5.2×10^{-3} $g.m^{-2}.d^{-1}$. Therefore, in this range, the dissolution rates are overall higher for experiments conducted in the saturation domain of CSH. Furthermore, the dissolution rates from short-term experiments range within one order of magnitude, regardless of the presence of CSH or not in the solution, while the dissolution rates from long-term experiments lie in the upper part of this range. As a consequence, two conditions seem to be required to observe enhanced ISG dissolution rates at high at $[SiO_2(aq)]/ [SiO_2(aq)]_{eq}$ ratios: (i) Secondary precipitates are mainly or only made up of CSH and ii) the experiments have to last longer than 20 days. This assertion has been confirmed by running Student's *t*-tests to test whether the difference between various rate data were statistically significant (see Supplementary Table S3). For $[SiO_2(aq)]/ [SiO_2(aq)]_{eq} >$ 9 %, the results of this analysis confirmed that the rate data collected in presence of CSH for long-durations are statistically different from (i) the rate data collected without CSH in the present study and (ii) the rate data from Fournier et al. (2019), whereas the rate data collected in the present

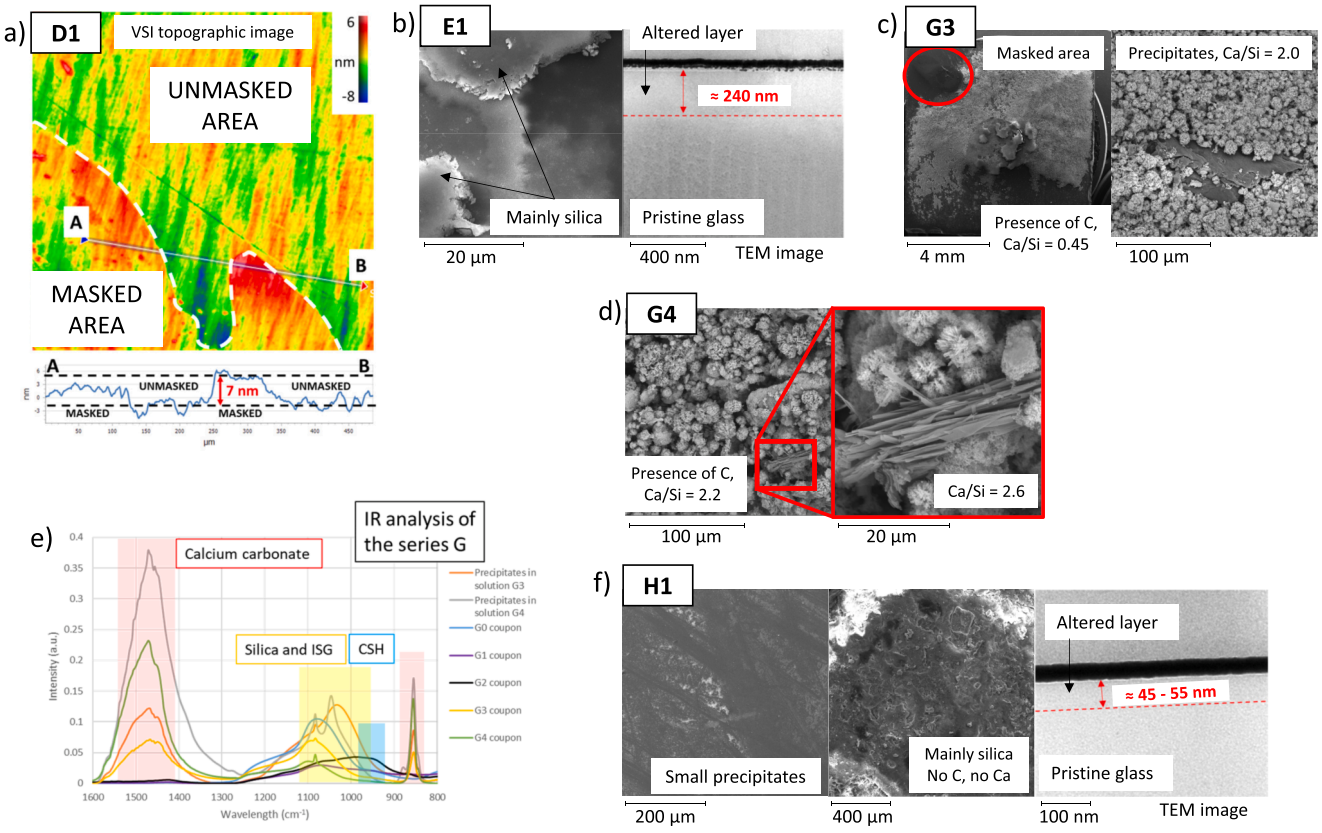

Fig. 6. Representative SEM, EDX and VSI characterizations of solids recovered from various experiments with a high $[SiO_2(aq)]$/ $[SiO_2(aq)]_{eq}$ ratio after 20 days at pH 10, 90 °C. a) VSI picture of D1 surface coupon that is representative of experiments run in the high $[SiO_2(aq)]$/ $[SiO_2(aq)]_{eq}$ ratio domain. The step between the reacted area and the non-reacted area was below 7 nm. b) SEM and TEM pictures of E1 coupon surface. c) and d) SEM pictures of G3 and G4 coupon surface, respectively. Calcium was exceptionally introduced in those two reactors under the form of calcium carbonates. e) IR analysis on the series G. The orange, grey, blue, violet, yellow and green lines correspond to the precipitates in the solution from G3 and G4, and the analysis of the surface of G0, G1, G3 and G4, respectively. The red, yellow and blue areas respectively indicate the domains where the peak of calcium carbonate, silica, ISG, and CSH with a ratio from 0.66 to 1.46 are expected. See Supplementary Note 3 for detailed band assignments to vibrational modes in this wavelength range. f) SEM and TEM pictures of H1 coupon surface. The precipitates on the surface of the coupon were too small to be analyzed by EDX. Neither C nor Ca was detected. (For interpretation of the references to colour in this figure legend, the reader is referred to the web version of this article.)

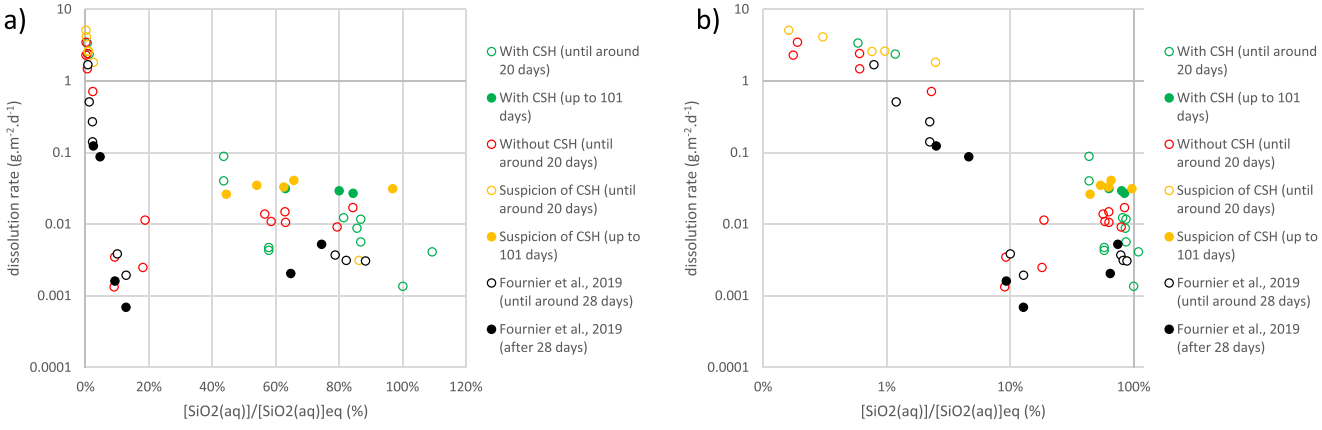

Fig. 7. Plots representing the dissolution rate of ISG in $g.m^{-2}.d^{-1}$ as a function of the $[SiO_2(aq)]$/ $[SiO_2(aq)]_{eq}$ ratio (%) and of the presence of CSH in the precipitates. Green open and filled circles correspond to experiments where CSH were positively found in the precipitates at the end of the 20-days and 101-days experiments, respectively. Red circles correspond to experiments where CSH did not precipitate until the end of the 20-days experiments. Yellow open circles and yellow filled circles correspond to experiments where CSH precipitation was highly suspected at the end of the 20-days and 101-days experiments, respectively. Black open circles and black filled circles refer to short-term and long-term (respectively) dissolution rates calculated from the data of Fournier et al., 2019 [14], corresponding to experiments where no secondary precipitate was observed. Both (a) and (b) refer to the same dataset, where (b) corresponds to a semi-log representation to better emphasize the results from experiments run at low Si concentrations. (For interpretation of the references to colour in this figure legend, the reader is referred to the web version of this article.)

study without CSH (or with CSH for durations < 20 days) are not statistically different from those collected by Fournier et al. (2019).

3.5. Longer-term experiments, relation between secondary precipitates and ISG dissolution rate

As described previously, the experiments were designed so as to minimize the impact of CO_2 on the chemical composition of fluid (and hence, on ISG reactivity) at the start of the experiments. The protocol adopted in this study proved successful for durations lasting up to ~3 weeks. Over longer durations, the penetration of CO_2 in the reactor was large enough to modify the sequence of precipitates. In this section, we present results of long-term experiments aimed at getting insights into the impact of the competition between CSH growth and carbonate precipitation on ISG dissolution rate.

The series I and J were designed to alter the ISG coupon under similar conditions: the solution was saturated with respect to amorphous silica and a significant amount of Ca was added initially in the reactor to reach 340 ppm of Ca for I3 and J3, and 620 ppm for I4, J4 and J4bis. The main difference between both series was that the solution was sampled only at the beginning and at the end of the experiment of J series in order to minimize handling of the reactor and accordingly, decrease the risk of carbonation (which eventually proved unsuccessful). Conversely, the series I was sampled regularly to monitor the evolution of the solution composition.

From the Fig. 8, the initial and final chemical compositions of the solution are similar between both series. As J4bis is a duplicate of J4, its solution chemical composition was not reported. The series I reveal that the activity of SiO_2(aq) in the solution first decreased, followed by both an increase in SiO_2(aq) activity and a decrease in the $(Ca^{2+})/(H^+)^2$ activity ratio. Initially, the solution is supersaturated with respect to CSH1.6, while at the end of the experiment, the solution is at equilibrium with respect to CSH0.8. Regarding the evolution of the pH of the solution, an acidification was observed for all experiments. Every solution was initially adjusted to pH 10.1 but after 101 days of alteration, the pH decreased to 9.9 and 9.5 for I3 and I4 respectively, with a measure of 9.8 for I4 at 89 days. Regarding the series J, the pH decreased to 9.7 for both J2 and J3, and to 8.9 and 9.0 for J4 and J4bis, respectively.

The evolution of the concentration of B, Ca and Si in the solution of I3 and I4 is reported in Fig. 8b–d. During the first 12 days, the B concentration observed a minute increase, while the concentration of Ca and Si remained constant, within uncertainties. Between 12 and 19 days, the concentration of Ca and Si decreased simultaneously. The decrease in Ca concentration represented 107 ppm and 138 ppm for I3 and I4, respectively, while the decrease in Si concentration represented 649 ppm and 744 ppm for I3 and I4, respectively. Between 19 and 76 days, the concentration of B in the solution significantly increased by about one order of magnitude (from 0.09 ppm to 0.87 ppm for I3 and from 0.09 ppm to 0.63 ppm for I4) whereas the concentration of Ca remained constant for both experiments. The concentration of Si in experiment I4 decreased significantly by a 2.7-factor, from 2500 ppm to 900 ppm while it only slightly decreased for I3. Between 76 and 89 days, the remaining amount of Ca in the solution precipitated, as suggested by the drop in Ca concentration. The concentration of B in the solution steadily increased,

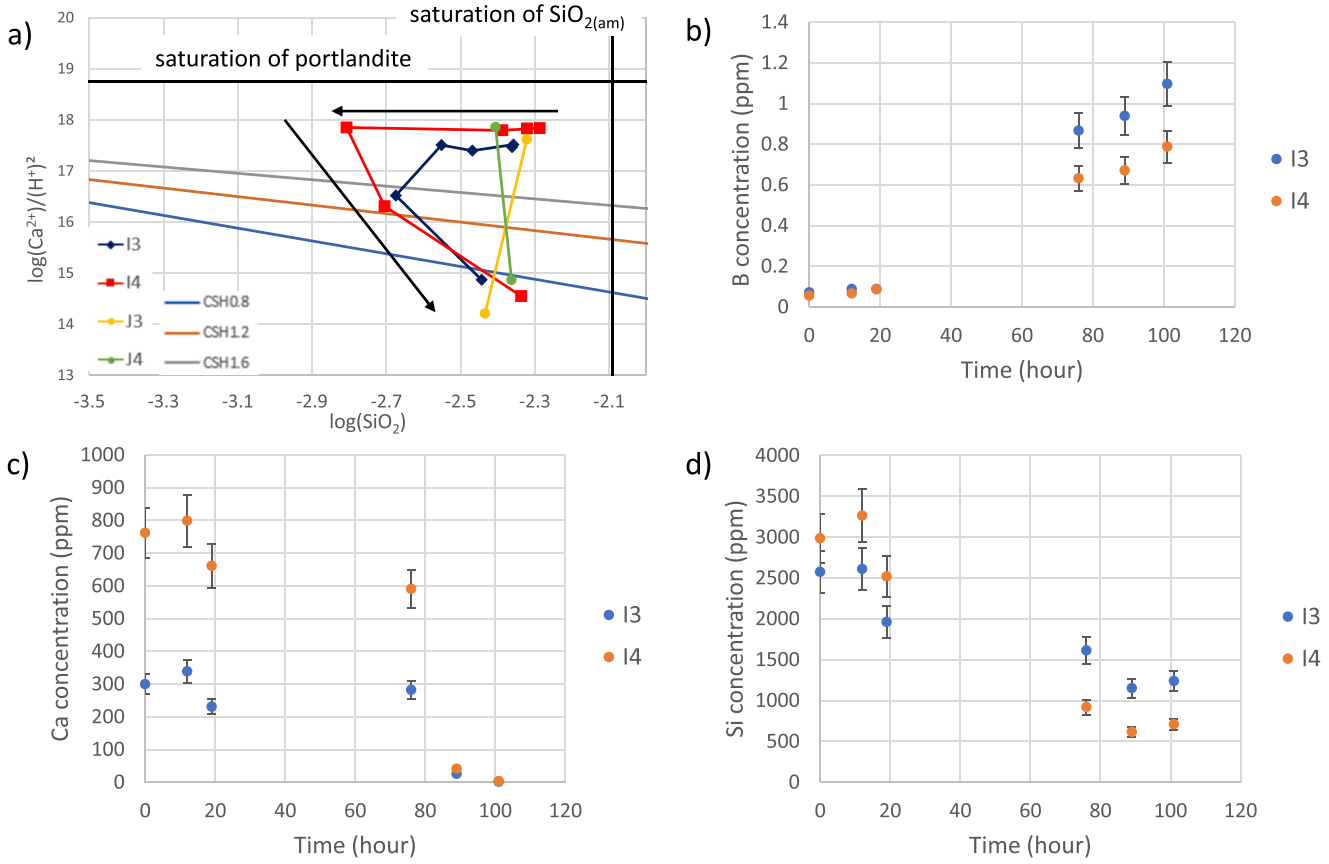

Fig. 8. Main results of fluid characterizations for series run over long (~3 months) durations (i.e., series I, J). (a) Activity diagram for the system CaO-SiO_2–H_2O representing the chemical composition of the solution for experiments I3, I4, J3 and J4. The blue, orange and grey lines represent the saturation lines of CSH0.8, CSH1.2 and CSH1.6 respectively. The black horizontal line corresponds to the saturation line with respect to portlandite and the black vertical line corresponds to the saturation line with respect to amorphous silica. The plots reported in b), c) and d) represent the evolution of the concentration of dissolved B, Ca and Si respectively, as a function of time (days) for the experiment I3 (blue circles) and I4 (orange circles). (For interpretation of the references to colour in this figure legend, the reader is referred to the web version of this article.)

but with a much slower pace and the concentration of Si decreases slightly. Finally, between 89 and 101 days, the concentration of Ca decreased to a few ppm for both series while the amount of Si remained constant. The concentration of B kept increasing at a slower rate.

The precipitates of those series that were found at the surface of the glass coupons were analyzed by EDX-SEM. Representative images are reported in Fig. 9. The picture and EDX characterization in Fig. 9a are characteristic of the others ISG coupons from series I and J collected at the end of the experiments. The common observation is a low Ca/Si ratio at 0.26 to 0.45 for experiment I4, around 0.7 for J4, and between 0.44 and 0.67 for J4bis. Such Ca/Si ratios were typically found on the surface of ISG coupons or precipitates after alteration in a (Ca, Si)-rich solution.

The precipitates on the glass surface shown in Fig. 9b presented two morphologies with two distinct values of Ca/Si ratios. The first one, with a Ca/Si value of 0.7 on average, presented an amorphous gel-like morphology whereas the second one, with a higher Ca/Si value of 1.1 on average, exhibited layers of euhedral crystals. Finally, another type of precipitates was present in J4bis that resembled cauliflowers and grew out of the amorphous gel-like precipitates. Both the amorphous and cauliflowers precipitates were characterized by TEM (Fig. 10b and c). Electron diffraction was performed on both precipitates and revealed an amorphous structure for the early precipitates (Fig. 10e) and a crystalline structure for the subsequent ones (Fig. 10d). The d-spacing measured on this image was as follow: 7.41 Å, 4.48 Å, 3.85 Å, 3.48 Å, 2.90 Å, 2.79 Å, 2.44 Å, 2.06 Å and 1.74 Å. EDX spectra on both precipitates showed that they both contain carbon, a significant amount of silicon and some calcium. The amount of calcium in the crystalline precipitates was higher, with Ca/Si ratio reaching up to 0.36, whereas the amorphous precipitates had a Ca/Si ratio of 0.06.

Below, we first examine the extent to which ISG dissolution rate can be predicted using the well-known first order dissolution rate law proposed by Grambow (2001) [57], which links glass dissolution rate to SiO_2(aq) activity. Then the impact of the calcium concentration was studied, with a specific emphasis on the impact of CSH formation. The chemical evolution of I3 and I4 solutions allowed us to further understand the different stages of evolution of the glass dissolution rate, which can be related to the maturation of CSH precipitates in the solution. Finally, the alteration mechanism of ISG was addressed. In particular, the dissolution rate evolution exhibited a resumption of alteration after 20 days, which may be attributed to an intrinsic evolution of the transport properties of the gel layer and/or its consumption by CSH precipitates.

4. Discussion

To unravel the reactivity of ISG at basic pH conditions in solutions enriched with dissolved Si and Ca, our dataset was compared to that of Fournier et al. (2019) [14], which was collected at the same temperature and similar pH conditions, but in Ca-low concentration solutions.

4.1. Relation between ISG dissolution rate and SiO_2(aq) concentrations

The rate and mechanisms of borosilicate glass dissolution has been studied for over 50 years [15,18,57-64]. In their study, Grambow et al., 1985 [65] and Grambow et al., 2001 [57] proposed a general dissolution rate law, based on the work of Aagaard et al., 1982 [66], which is often referred to as 'first order dissolution rate law'. A simplified equation of this rate law is reported in Eq. (4):

$$r_{diss} = k(T) \times \left(1 - \frac{a_{SiO2(aq)}}{K_{SiO_2}(T)}\right) \quad (4)$$

where $k(T)$ is a rate constant ($g.m^{-2}.d^{-1}$) that depends on the temperature T (K) and $K_{SiO_2}(T)$ is the solubility constant at the dissolving glass surface, which depends on the temperature.

This law ensures that when the solution is highly undersaturated with respect to amorphous silica, the dissolution rate of the borosilicate glass (r_{diss}), is equal to the forward dissolution rate, r_0, which corresponds to a maximum for a given set of T and pH conditions. When the solution approaches the saturation of the gel (approximated to that of amorphous silica for instance), the dissolution rate is supposed to drop down to zero. Note that similar rate laws proved satisfactory to describe the reactivity of some silicate minerals [67-69] and basaltic glass [70]. The rate law can be refined using the actual solubility of the gel layer instead of that of SiO_2(am) [14,71-73]. However, above that threshold, a residual dissolution rate was observed as the (boro)silicate glass kept dissolving beyond saturation [74-76]. Mechanisms behind the residual rate are still debated within the community [64]. One of the hypotheses is that the reaction is controlled by the ingress of reactants and products through the gel layer [68,77].

In the present study, when the solution was saturated with respect to amorphous silica, which is the most soluble polymorph of SiO_2, the dissolution rate of ISG reached a minimum for two reasons: (i) the chemical affinity between the solution and the solid was the lowest [24, 78] and (ii) possibly, a passivating layer formed in alkaline pH [9]. These two mechanisms are additive. The latter mechanism can be mitigated or annihilated by the precipitation of secondary silicate phases, such as zeolites or CSH [15,79].

The dissolution rates calculated in this study, and that of Fournier

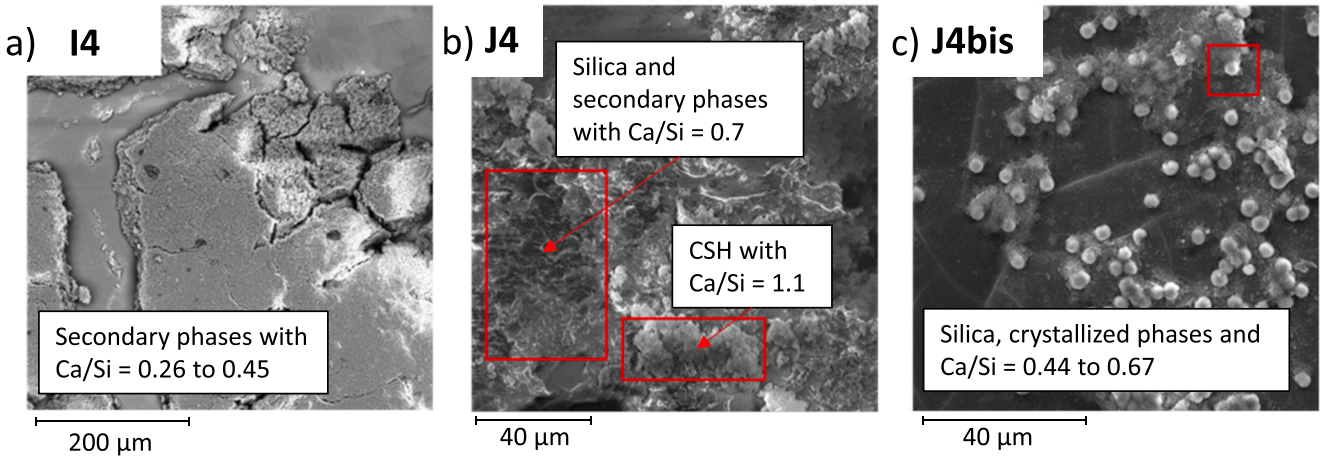

Fig. 9. SEM characterizations of the surface of ISG coupons after 101 days of alteration from the experiment a) I4, b) J4 and c) J4bis at 90 °C, and an initial pH of 10.1.

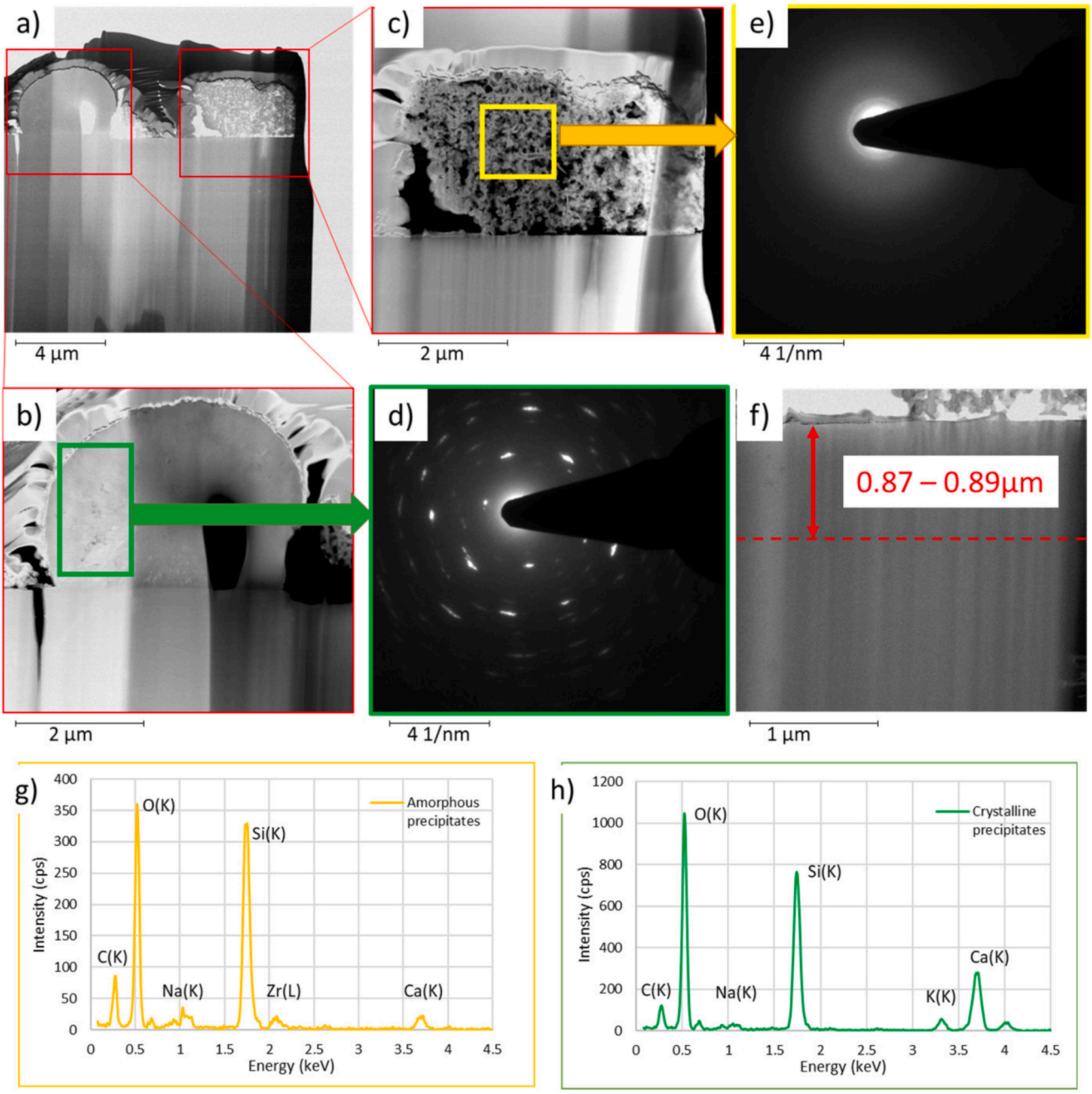

Fig. 10. FIB-TEM characterization of the ISG coupon surface and associated precipitates from J4bis experiments, collected after 101 days of alteration at pH 10.1. The composition of both crystalline and amorphous precipitates was obtained by STEM-EDX. a) TEM bright field image of the surface with both crystalline precipitates on the left and amorphous precipitates on the right. b) and c) TEM dark field close up views on the crystalline precipitates and the amorphous precipitates respectively. d) and e) Electron diffraction of the crystalline precipitates and the amorphous precipitates respectively. f) TEM image of the surface, showing that the thickness of the gel layer ranges between 0.87 and 0.89 µm. This observation was supported by STEM-EDX map of the area at the Ca K edge, K edge, Na K edge, Si K edge and Al K edge (not reported). g) and h) EDX spectra collected on the crystalline precipitates and the amorphous precipitates respectively.

et al. (2019) [14] were compared with the first order dissolution rate law in Fig. 11b, where the rate plateau corresponding to the forward rate r_0 was set to 11.2 $g.m^{-2}.d^{-1}$ according to the study of Fournier et al. (2016) [80]. As can be seen in Fig. 11b, the general trend depicted by the rate data does not follow the first order dissolution rate law.

A correction to the first order dissolution rate law was then applied, by adjusting the solubility limit of SiO_2, considering that the gel layer is less soluble that amorphous silica because of the presence of Al [26]. In order to apply this correction, two different domains of dissolution rate were drawn based on $[SiO_2(aq)]/ [SiO_2(aq)]_{eq}$ ratio. The first one corresponds to a high dissolution rate, > 1 $g.m^{-2}.d^{-1}$, when $[SiO_2(aq)]/ [SiO_2(aq)]_{eq}$ is below 2 % and a second one that corresponds to a low dissolution rate, < 0.1 $g.m^{-2}.d^{-1}$, where $[SiO_2(aq)]/ [SiO_2(aq)]_{eq}$ is greater than 9 %. These two domains were supported by solid characterization and VSI analyses (Figs. 5 and 6). The significant surface retreat revealed by VSI characterization (up to 33 µm) and the very thin (a few 100 s of nm at most according to the solution analyses) gel layer testified that the solution was very far from the solubility of the gel layer. Conversely, the surface retreat was very low for $[SiO_2(aq)]/ [SiO_2(aq)]_{eq}$ ratios ranging from 9 % to 18 % (< 20 nm) and below the VSI quantification limit (< 2 nm) for $[SiO_2(aq)]/ [SiO_2(aq)]_{eq}$ ratios greater than 44 %. For $[SiO_2(aq)]/ [SiO_2(aq)]_{eq}$ ratios between 9 % and 18 % (series

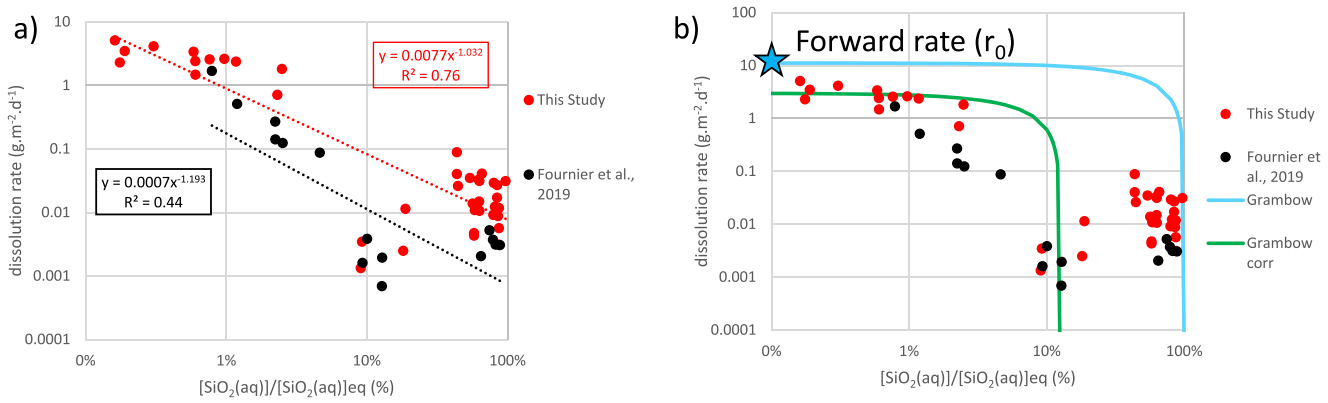

Fig. 11. Glass dissolution rate ($g.m^{-2}.d^{-1}$) as a function of $[SiO_2(aq)]/ [SiO_2(aq)]eq$. The red circles correspond to the data from this study. The black circles correspond to the data from Fournier et al., 2019 [14]. a) Dissolution rate and $[SiO_2(aq)]/ [SiO_2(aq)]eq$ is represented with a linear regression on both data set. b) Both data sets are compared with the first order alteration law from Grambow et al., 2001 [57]. The blue line refers to the original first order alteration law and the blue star corresponds to the forward dissolution rate in Fournier et al., (2016) [80]. The green line refers to a first order law corrected by the solubility of the gel layer based on this study and the best forward dissolution rate based on this study. (For interpretation of the references to colour in this figure legend, the reader is referred to the web version of this article.)

D), the surface retreat was between 10 and 20 nm. In this latter domain, the thickness of the gel layer, calculated based on ToF-SIMS, FIB-TEM or even ICP-OES, were on the same order of magnitude after 20 days of alteration (a few tens of nanometers up to a hundred nanometers). These observations suggest that the solubility of the gel layer is lower than that of SiO_2(am) and may be around 12 % of SiO_2(am) saturation (Fig. 11), in reasonable agreement with the apparent solubility reported in Gin et al. (2012) at pH = 9 (~20 % of SiO_2(am) saturation). Of note, the threshold where the alteration process switches from hydrolysis-controlled mechanism ($[SiO_2(aq)]/ [SiO_2(aq)]_{eq} < 9$ %) to diffusion-controlled mechanism ($[SiO_2(aq)]/ [SiO_2(aq)]_{eq} > 9$ %) lies in the range of the solubility of quartz, which is the most insoluble silica phase (17 % of SiO_2(am) saturation).

Interestingly, the low dissolution rate (< 0.01 $g.m^{-2}.d^{-1}$) reported by Fournier et al. (2019) [14] for experiments carried out with a $[SiO_2(aq)]/ [SiO_2(aq)]_{eq}$ between 9 % and 13 % is an additional independent argument supporting that the apparent solubility for the passivating gel layer formed on ISG ranges from 9 % to 18 % of that of amorphous silica at pH 10 and 90 °C.

Finally, in addition to the concerns regarding the gel layer solubility, the first order dissolution rate law does not capture the far-from-equilibrium rates ($[SiO_2(aq)]/ [SiO_2(aq)]_{eq}$ <2 %) reported both in the present study or that of Fournier et al. (2019) [14]. Indeed, the dissolution rates in this domain can be up to one order of magnitude lower. Furthermore, the rate data from Fournier et al. (2019) [14] steadily decreases with increasing SiO_2(aq) concentrations, without describing an initial rate plateau (Fig. 11b). A reasonable agreement can be highlighted from the dissolution rates in this study with the corrected first-order dissolution rate law when considering a lower forward dissolution rate of around 3 $g.m^{-2}.d^{-1}$. However, this law cannot explain the dissolution rates that are measured for saturation states exceeding 12 %.

To conclude, ISG dissolution rate is unquestionably negatively correlated with the increase in SiO_2(aq) activity in solution. While the data collected in the present study observe a rather linear correlation between dissolution rates and $[SiO_2(aq)]/ [SiO_2(aq)]_{eq}$ in a log-log plot (Fig. 11a) with a correlation coefficient of $R^2 \approx 0.76$, the rate data calculated from the experiments conducted by Fournier et al. (2019) [14] exhibit a weaker linear correlation ($R^2 = 0.44$). The observations collected in the present study support that ISG dissolution rate obeys a general empirical rate law related to the activity of silica in solution, although following a more complicated relation than the first order alteration rate law suggested by Grambow et al., (2001) [57]. The discrepancies above discussed are likely due to the fact that both the glass and the gel contain other elements than Si (Al, Zr, Ca) that impact the rate of hydrolysis of the glass matrix and the gel properties.

4.2. *Impact of aqueous Ca and Ca-bearing secondary phases on ISG dissolution rate during short-term experiments*

After analyzing the effect of Si on the dissolution rate, the effect of calcium was investigated. As calcium may play a role in the transport properties of the gel layer formed on ISG [9,11], the rate data were plotted as a function of the concentration of calcium in solution, for all experiments conducted in the domain where the solution composition exceeds the solubility of the gel layer (i.e., $[SiO_2(aq)]/ [SiO_2(aq)]_{eq} > 9$ %). For Ca concentrations covering a range of ~5 orders of magnitude, the dissolution rate did not appear to be correlated with the concentration of calcium in solution (Supplementary Fig. S4). This observation contrasts with results obtained on short-term experiments, where the heterogeneous precipitation of CSH at the surface of ISG was weak or absent. In the latter case, a 33 % decrease in the rate was observed when the concentration of Ca was increased from 0 to 250 ppm (G series; results being discussed at length in an upcoming study).

The investigation thus focused on the impact of Ca-bearing secondary phases such as CSH and calcium carbonates. To unravel their effect on the dissolution rate, the experiments in this study where calcium was added to the onset solution were compared to the experiments of Fournier et al. (2019) [14], where Ca-free solutions were employed.

The dissolution rates calculated by Fournier et al. (2019) [14] are lower than the ones calculated in this study (Fig. 11a) by about an order of magnitude (intercept of the linear regression slope is log(0.0007) = −3.15 for the data from Fournier et al. (2019) [14] and log(0.0077) = −2.11 for this study). Focusing on the experiments with a $[SiO_2(aq)]/ [SiO_2(aq)]_{eq}$ ratio > 9 % for both studies, some discrepancies can be highlighted. Despite the correlation between the dissolution rate and the activity of silica in solution, S2-Blk-9.8 experiment (conducted with a $[SiO_2(aq)]/ [SiO_2(aq)]_{eq}$ ratio around 10 %) exhibits a dissolution rate that is lower (< 0.01 $g.m^{-2}.d^{-1}$) than some experiments conducted in the present study with a $[SiO_2(aq)]/ [SiO_2(aq)]_{eq}$ ratio between 44 % to 100 % (0.01 $g.m^{-2}.d^{-1}$< dissolution rate < 0.1 $g.m^{-2}.d^{-1}$).

Because no correlation was found between dissolved calcium concentrations and the glass dissolution rate, the hypothesis that CSH are the source of the discrepancies between the rate data collected by Fournier and coworkers and the results from the present study was therefore investigated next. As a reminder, no secondary precipitates were reported in the datasets selected from Fournier et al. (2019) [14], whereas most rate data collected in the present study at $[SiO_2(aq)]/$

$[SiO_2(aq)]_{eq}$ > 44 % were obtained in the saturation domain with respect to CSH0.8 and/or CSH1.2 and/or CSH1.6.

The precipitates formed in our experiments were characterized using IR and SEM-EDX to determine their composition and nature. Considering the temperature of 90 °C, the pH around 10 and the Si and Ca chemical composition of the solution, three different secondary phases were mainly expected: (i) amorphous silica, as it corresponds to the SiO_2 polymorph with the highest precipitation rate in this range of temperature; (ii) CSH, as the experiments were designed to favor the precipitation of these minerals [27], and (iii) calcium carbonates in case the solution got in contact with the atmosphere and CO_2 dissolved in the solution [38,40,41,48]. Some other phases such as zeolites might precipitate but as minor phases (see Ferrand et al., 2021 [27] for more details), and were not evidenced from our experiments. Conversely, amorphous silica, CSH and calcium carbonates precipitates were actually evidenced in the present study (see Results and Figs. 5 and 6).

A clear increase in dissolution rate was observed only when CSH precipitated in experiments lasting >20 days (see Fig. 7). As little to no difference was highlighted from the short-term experiments dissolution rate with or without CSH (Fig. 7), an induction period, here lasting around 20 days, seems to be required for CSH precipitation to significantly impact ISG reactivity. According to Mercado-Depierre et al. (2013) [9], the precipitation of CSH lowers the activity of SiO_2(aq), and the glass dissolution rate is expected to be equal to the forward dissolution rate, at the maximum.

To conclude, the presence of CSH has little to no effect on the dissolution rate for short-term experiment and increases the dissolution rate for longer-term experiment, up to one order of magnitude. However, the increase is only of second order compared to the effect of the activity of aqueous silica in the solution.

4.3. Alteration mechanism and dissolution resumption, insight from 101 days alteration experiments

After addressing the impact of dissolved Si and Ca, and Ca-precipitates on ISG dissolution rate over short-time experiments, we here attempt to determine the rate-controlling processes and associated mechanisms of ISG dissolution based on long-term experiments. In that respect, experiments labelled I3 and I4 were carried out over 101 days and were submitted to time-resolved aqueous sampling (Fig. 8). To verify that this sampling did not disturb the progress of the experiments, J3 was prepared as a replicate of I3, and J4 and J4bis were prepared as replicates of I4, although none of these replicates experienced time-resolved aqueous sampling (the corresponding reactors remained closed until the end of the experiments). The starting and final compositions of the fluid were found similar, suggesting a similar fluid evolution in all experiments (Fig. 8a).

These experiments, and especially I3 and I4, were compared to S2-Sat-9.8 and S2-Blk-9.8 from Fournier et al. (2019) [14], for which the experiments lasted up to 379 days. For the record, all these experiments were run at high $[SiO_2(aq)]/ [SiO_2(aq)]_{eq}$, corresponding to conditions where the passivating layer was not supposed to dissolve (see above). In these conditions, the dissolution of ISG is typically thought to be diffusion-controlled [24,78]. To test this hypothesis, the equivalent thickness calculated from long-term experiments were fitted following:

$$Eth = \frac{2}{\sqrt{\pi}}\sqrt{D_{Fick} \times t} \quad (5)$$

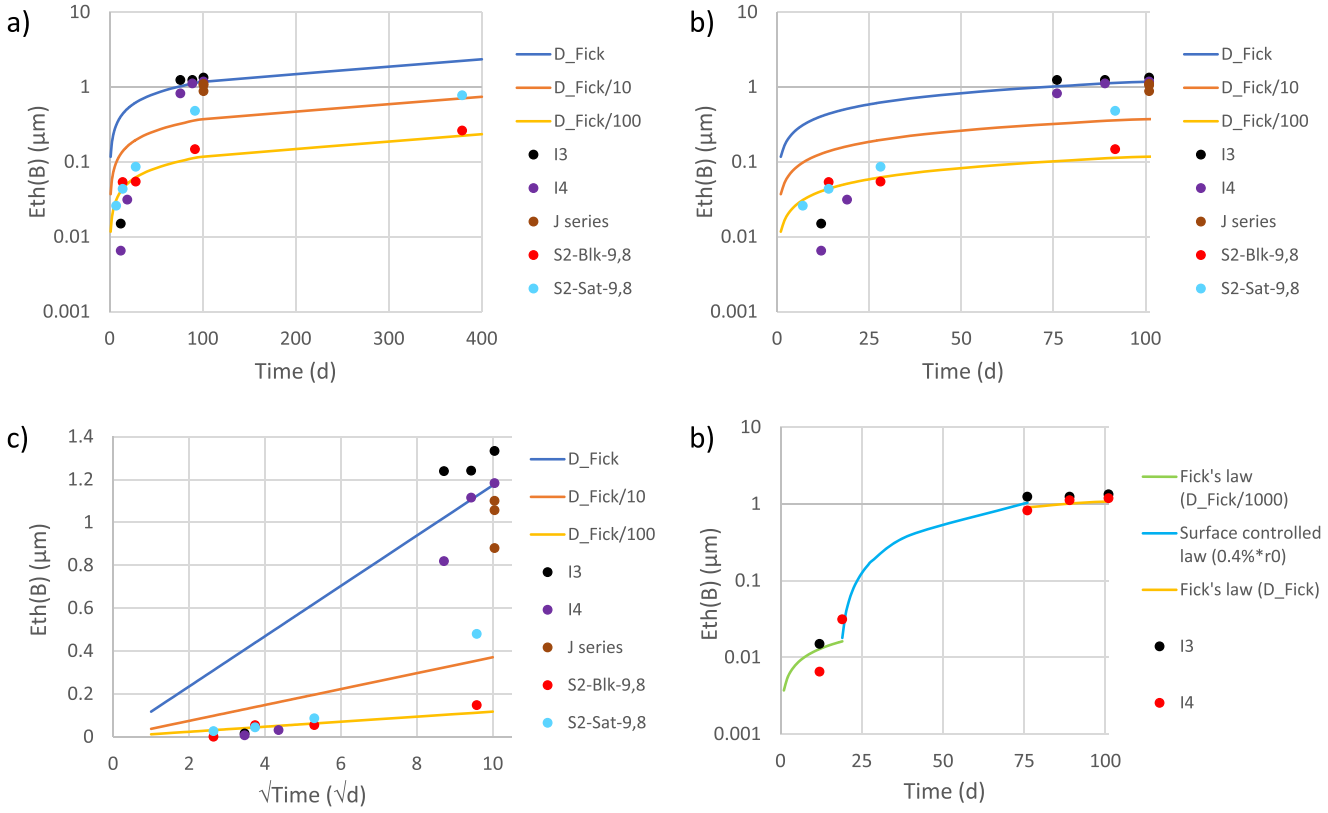

Fig. 12. Plots representing the gel layer thickness (µm) based on the release of B in the solution as a function of time (day). a) and b) represent the dissolution rate of a few selected experiments. The experiment duration is up to a) 379 days for Fournier's data. Conversely, the experiments were stopped after b) 101 days in the present study. The dissolution rate is compared to the diffusion-controlled dissolution rate established by Fick's law. The diffusion coefficient is $D_{Fick} = 1.78 \times 10^{-19}$ $m^2.s^{-1}$ from Gin et al., 2020 [64]. The other curves refer to a lower diffusion coefficient. c) is another representation of b). d) models of the dissolution rate evolution by combining Fick's law and the forward dissolution rate of ISG sample that is of $r_0 = 11.2$ $g.m^{-2}.d^{-1}$ from Fournier et al., 2016 [80]. This forward dissolution rate is, however, adjusted to only 0.4 % of r0.

where t corresponds to the time in days and D_{Fick} refers to a diffusion coefficient extrapolated from Gin et al., 2020 [64] and is equal to 1.8 × 10^{-19} $m^2.s^{-1}$ at pH 10.

On the one hand, the experiments carried out by Fournier et al. (2019) [14] are in reasonable agreement with a diffusion-limited regime throughout the duration of the experiment, although the diffusion coefficient (D_{Fick}) is one (S2-Sat-9.8) to two (S2-Blk-9.8) orders of magnitude lower than the one extrapolated from Gin et al., 2020 [64] (Fig. 12a and b).

On the other hand, the release of B from experiments I3 and I4 followed a more complex evolution:

- For durations shorter than 20 days, the release rate of B is close to (or even lower than) that observed from experiments S2-Sat-9.8 and S2-Blk-9.8 (Fig. 12a–c).
- A sudden increase in the calculated equivalent thickness is then observed (Fig. 12a and b) between 19 days and 76 days, as the experimental data points deviate from the Fickian trend described for time ranging from 0 to 19 days (Fig. 12c).
- Finally, for durations longer than 76 days, the concentration of B keeps increasing, though to a much lower pace. In parallel, no retreat at the surface of the coupon was measured with VSI in areas devoid of secondary phases. In addition, the precipitates from J4 and J4bis presented both silica gel with a Ca/Si ratio of 0.7, CSH precipitates with a layer-like morphology and a Ca/Si ratio of 1.1 at the surface of ISG sample, and faceted CSH with a Ca/Si ratio between 0.44 and 0.67 (Fig. 9b and 9c). The FIB thin section prepared on J4bis coupon positively supports the presence of both amorphous silica (Fig. 10e and 10g), calcium carbonate (as inferred from the presence of Ca and C in the precipitates, Fig. 10g), and CSH, as the electron diffraction pattern shown in Fig. 10d is in good agreement with the d-spacing of okenite (Ca_3 [Si_6O_{15}]●$6H_2O$) (7.66 Å, 4.53 Å, 3.97 Å, 3.49 Å, 2.92 Å, 2.80 Å and 2.39 Å) [81]. Okenite is known to be a crystallized CSH that is highly keen to precipitate during ISG dissolution in hyperalkaline condition at 70 °C [27,39,45].

Based on the abovementioned observations, we suggest the following scenario to describe the reactivity of ISG in a (Si, Ca)-rich environment at 90 °C and alkaline conditions (Fig. 13):

(1) First, the precipitation of CSH occurred at the very moment of Ca addition in the solution and was visually observed through the turbidity of the solution, which increased with the amount of added Ca. This first precipitation step corresponds mainly to homogenous CSH nucleation in the solution, as inferred from the analyses of the solids filtered from the solution (see e.g., Fig. 5a). This nucleation marked the first step of CSH formation, as described in the literature [33,35]. Small CSH clusters then aggregated slowly and started growing layer by layer before a potential crystallization. This aggregation and growth represented the second step of CSH nucleation [35], which occurred in this study between 12 days and 19 days, as suggested by the sudden decrease in aqueous Ca and Si concentrations in series I and J (Fig. 8). However, even if the loss of Ca and Si concentrations was similar in both experiments, the corresponding aqueous Ca/Si ratio suggested (0.12) that a significant amount of amorphous silica precipitated along with the CSH. The SEM images of A3 experiment confirmed the precipitation of both phases (e.g., Fig. 5a). As CSH precipitates were formed mainly in the bulk solution while the [SiO_2(aq)]/ [SiO_2(aq)]$_{eq}$ ratio did not decrease down to the solubility limit of the gel (suggested to be close to 9 %

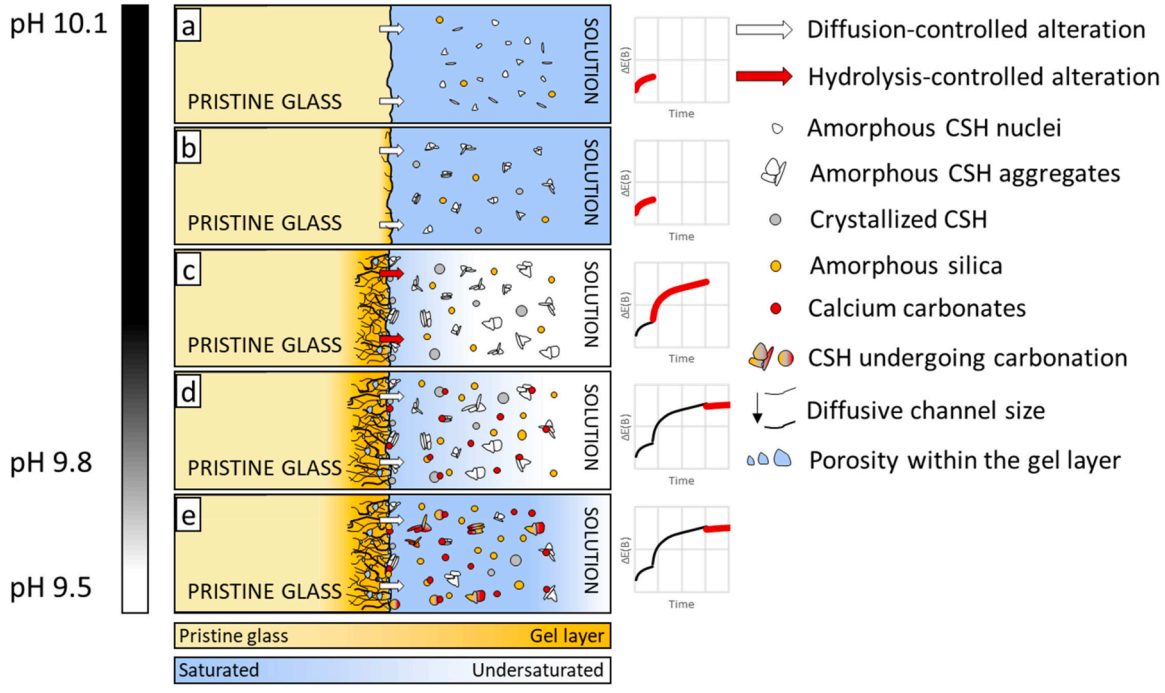

Fig. 13. Schematic summary of the proposed ISG alteration process in a (Ca, Si)-rich solution and pH 10, with possible influence of CO_2. a) After the addition of Ca in the pH 10.1 saturated solution with respect to amorphous silica, homogeneous precipitation of CSH occurs. The alteration of ISG is diffusion-controlled. b) During the first 20 days, CSH aggregate and gradually crystallize. c) The dissolution rate increases by a x15 factor. The alteration mechanism switches from diffusion-controlled to hydrolysis-controlled during the growth of the CSH. In spite of glass dissolution, the concentration of silica in the solution decreases due to CSH consumption and amorphous silica precipitation. The solution becomes locally undersaturated with respect to the gel layer. Until the end of the CSH growth, the pH remains mostly constant. d) After 76 days, the pH starts to decrease (ingress of CO_2). Calcium carbonates precipitate at the expense of CSH and Ca in solution. The dissolution rate decreases, and the alteration mechanism shifts back to a diffusion-limited process. Since the pH has decreased, the solution approaches the solubility of amorphous silica. e) CSH start to undergo a carbonation process with amorphous silica and calcium carbonates as by-products. The pH keeps decreasing, bringing back the solution close to the saturation state with respect to amorphous silica. The alteration remains diffusion-controlled.

of the solubility od amorphous silica in this study), the precipitation of CSH had only a very modest impact on ISG dissolution rate, which was similar to or slightly higher than the dissolution rates from Fournier et al. (2019) [14], measured in absence of precipitates (Figs. 7 and 11).

(2) For durations exceeding ~20 days, CSH also started to aggregate and grow at the surface of the ISG coupons (Figs. 6, 9, 10). The resumption of glass alteration revealed in Fig. 12 may be ascribed to the precipitation of CSH at the expense of passivating gel. Considering that if the alteration was only diffusion-controlled, no resumption of evolution would have been observed, a shift in the rate-controlling process from transport-limited to hydrolysis-limited may be proposed (Fig. 12d). This shift was supposedly due to i) the dissolution or consumption of the gel layer locally by the CSH precipitates, allowing a faster alteration from the opening of the porosity within the gel layer and ii) the local shift of the solution away from amorphous silica saturation. Supporting this assertion, the dissolution rate between 19 and 76 days increased up to around 15x compared with the dissolution rate between 0 and 19 days, which is in reasonable agreement with previous findings. According to Fournier et al., 2017 [82], the precipitation of secondary phases at pH 10 could raise ISG dissolution rate up to 10^{-2} $g.m^{-2}.d^{-1}$, which remains much lower than r_0 at the corresponding pH of 10. Although the phases that precipitated in Fournier's study were zeolites instead of CSH, it gives an indicative value of the glass dissolution rate controlled by secondary silicate phases precipitation. Thus, it seems reasonable to observe a resumption of alteration at a quite low dissolution rate relative to r_0.

In addition, our study suggests that the impact of CSH must have remained local (i.e., at the contact between CSH and the surface of the altered coupon), since the Si concentration in the bulk solution remained such that $[SiO_2(aq)]/[SiO_2(aq)]_{eq} > 9$ %, which is a reasonable estimate for the solubility of the passivating gel layer (in other words, the decrease in the bulk aqueous Si concentration could not account for a such a drastic resumption of ISG dissolution). This suggestion would be supported by the observation that $r\_disso(B)$ from ICP-OES analyses were equal or greater in general than r_solid from solid characterization (Fig. 4), while the VSI analyses did not evidence any surface retreat (i.e., the consumption of the gel layer did not occur in areas devoid of secondary phases, and must have occurred below the CSH, which was impossible to probe with VSI). Of note, the resumption of the alteration due to the growth of secondary phases at the expense of the gel was also studied by Gin et al. (2015) [15]. After perturbating the environment by increasing the pH from 9 to 11.5, they observed the precipitation of CSH and zeolites that maintained the dissolution rate close to the forward dissolution rate until complete dissolution of ISG. However, contrary to Gin et al. (2015) [15], the forward dissolution rate was not reached during our study, likely because the pH was lower than in this previous study [82].

(3) Between 76 days and 89 days, the concentration of calcium in the solution decreased to a few tens of ppm, which represent between 9 % and 5 % of the initial concentration of calcium in the solution for I3 and I4, respectively. Because the evolution of Si in the solution did not correlate with that of Ca, the crystallization of CSH can be dismissed. As a drop in pH was observed during that time, the consumption of Ca most likely resulted from the precipitation of calcium carbonates phases, probably due to a slow dissolution of CO_2 in the solution, as the reactor is not fully impermeable. The ingress of CO_2 in the reactors in long-term experiments shifted the composition of the solution outside of the stability field of CSH that were formed at early stages (Fig. 8a), resulting in their transformation in favor of carbonate phases and amorphous silica, as confirmed by TEM observations (Fig. 10a). Ultimately, if the resumption of ISG dissolution observed between 19 and 76 days was due to the destabilization of the gel layer because of the growth of CSH, then the carbonation of CSH is a likely mechanism that could explain why ISG dissolution shifts back to a diffusion-controlled process, as the driving force for the gel layer destabilization has vanished.

As a conclusion, whereas ISG dissolution rate is negatively correlated to first order with the activity of dissolved silica in the solution, to second order, the precipitation of CSH in the solution has likely contributed to a transient increase in the dissolution rate, but not up to the forward dissolution rate (around 0.5 % of r_0). A hypothesis was proposed for this increase in the dissolution rate: the gel layer is dissolved or consumed locally by the CSH precipitates (Fig. 13).

5. Conclusion

While the mechanisms and kinetics of ISG dissolution have been extensively investigated over the past decade (Gin et al., 2018 [63] and references therein), the reactivity of ISG at basic pH and in (Ca, Si)-rich environment remained essentially unexplored. By studying the reactivity of ISG in alkaline condition at 90 °C with various dissolved calcium and silicon concentrations, the following conclusions can be drawn:

(i) The dissolution rate of ISG is strongly and negatively correlated with the activity of dissolved silica in the solution. The solubility of the gel layer may range between 2 % and 9 % of that of amorphous silica. Above that threshold, the dissolution rate remains low (< 0.1 $g.m^{-2}.d^{-1}$) and is diffusion-controlled.

(ii) The secondary phases, and in particular CSH precipitates, have only a second order effect on the dissolution rate of ISG during the first 19 days of alteration. These conclusions contrast with those offered by Mercado-Depierre et al. (2013) [9], who observed that the dissolution rate increases up to the forward dissolution rate as soon as the solution is saturated with respect to CSH.

(iii) A resumption of the glass dissolution rate is observed between 19 and 76 days. It can be explained by a shift in the alteration mechanism from diffusion to hydrolysis. However, the forward dissolution rate remains unattained.

(iv) The competition between the formation of CSH and calcium carbonates likely limited the resumption of ISG dissolution in the experiments conducted in the present study. For experiments run over durations exceeding 76 days, the precipitation of calcium carbonates consumed CSH while resulting in the acidification of the solution, which in turn was responsible for a shift in the solution composition towards conditions closer to amorphous silica saturation. As a consequence, the dissolution process returned back to a diffusion-limited regime, though with a diffusion coefficient higher than in the previous step of the process.

This study proposes a general understanding of borosilicate glass behavior in (Si, Ca)-rich environment under alkaline condition which is of interest concerning the present concepts of deep geological repository in France. One of the main concerns of the borosilicate glass dissolution in interaction with a cementitious grout is the alteration resumption due to secondary phases. The results presented here tend to confirm this concern, however, the presence of carbonates in solution might prevent or limit the resumption of glass alteration from CSH precipitates. Therefore, we suggest that in addition to the impact of dissolved Ca and Si, future studies should be directed at assessing the impact of carbonates and investigating the state of the altered glass after the alkaline alteration.

CRediT authorship contribution statement

Benjamin Cagnon: Writing – original draft, Investigation, Formal analysis. **Stéphane Gin:** Writing – review & editing, Supervision. **Martiane Cabié:** Formal analysis. **Damien Daval:** Writing – review & editing, Supervision.

Declaration of competing interest

The authors declare that they have no known competing financial interests or personal relationships that could have appeared to influence the work reported in this paper.

Data availability

Data will be made available on request.

Acknowledgements

The authors thank Simona Denti (ISTerre), Delphine Tisserand (ISTerre), Sylvain Campillo (ISTerre) and Sabine Santenac (ISTerre) for helping and providing advice with the ICP-OES analysis, Nathaniel Findling (ISTerre) and Rachel Martin (ISTerre) for teaching and providing assistance with the SEM-EDX characterizations. The authors are also grateful to Loan Lai, Elodie Chauvet, Amandine David, Florian Cousy and Yves Depuydt from Tescan Analytics for performing ToF-SIMS analyses and operating FIB thin sections. Nicolas Michau and Christelle Martin from Andra, and Theo Montaigne from EDF are thanked for their inputs on an earlier version of this manuscript. This work was funded by Andra and EDF. Finally, two anonymous reviewers are thanked for their suggestions which significantly contributed to clarify an initial version of this manuscript.

Author contributions

B.C. performed the experiments and analyzed data. M.C. performed and analyzed the TEM measurements as well as STEM-EDX characterization. D.D. and S.G. analyzed data and supervised the research. B.C., D. D., and S.G. wrote the manuscript, with contributions from all authors.

Supplementary materials

Supplementary material associated with this article can be found, in the online version, at doi:10.1016/j.jnucmat.2024.155426.

References

[1] M.I. Ojovan, W.E. Lee, Glassy wasteforms for nuclear waste immobilization, Metallurg. Mater. Transact. A 42 (2011) 837–851, https://doi.org/10.1007/s11661-010-0525-7.
[2] V.H.J.M.d. Santos, et al., Application of Fourier Transform infrared spectroscopy (FTIR) coupled with multivariate regression for calcium carbonate (CaCO3) quantification in cement, Construct. Build. Mater. 313 (2021) 125413, https://doi.org/10.1016/j.conbuildmat.2021.125413.
[3] P.F. Diane Rebiscoul, A.A. Stéphane Gin, Protective properties and dissolution ability of the gel formed during nuclear glass alteration, J. Nucl. Mater. 342 (2005) 26–34, https://doi.org/10.1016/j.jnucmat.2005.03.018.
[4] A. A. K. Ferrand, B. Grambow, Water diffusion in the simulated French nuclear waste glass SON 68 contacting silica rich solutions: experimental and modeling J. Nucl. Mater. 355 (2006) 54–67, https://doi.org/10.1016/j.jnucmat.2006.04.005.
[5] S. Gin, et al., Origin and consequences of silicate glass passivation by surface layers, Nat. Commun. 6 (2015) 6360, https://doi.org/10.1038/ncomms7360.
[6] S. Gin, et al., Atom-Probe Tomography, TEM and ToF-SIMS study of borosilicate glass alteration rim: a multiscale approach to investigating rate-limiting mechanisms, Geochim. Cosmochim. Ac. 202 (2017) 57–76, https://doi.org/10.1016/j.gca.2016.12.029.
[7] S. Gin, et al., An international initiative on long-term behavior of high-level nuclear waste glass, Mater. Today 16 (2013) 243–248, https://doi.org/10.1016/j.mattod.2013.06.008.
[8] Y. Inagaki, T. Kikunaga, K. Idemitsu, T. Arima, Initial dissolution rate of the international simple glass as a function of pH and temperature measured using microchannel flow-through test method, Int. J. Appl. Glass Sci. 4 (2013) 317–327.
[9] S. Mercado-Depierre, F. Angeli, F. Frizon, S. Gin, Antagonist effects of calcium on borosilicate glass alteration, J. Nucl. Mater. 441 (2013) 402–410, https://doi.org/10.1016/j.jnucmat.2013.06.023.
[10] T. CHAVE, P. Frugier, S. Gin, A. Ayral, Glass–water interphase reactivity with calcium rich solutions, Geochim. Cosmochim. Ac. 75 (2011) 4125–4139, https://doi.org/10.1016/j.gca.2011.05.005.
[11] M. Collin, M. Fournier, T. Charpentier, M. Moskura, S Gin, Impact of alkali on the passivation of silicate glass, npj Mater. Degrad. 2 (2018) 16.
[12] C. Utton, et al., Dissolution of Vitrified Wastes in a High-pH Calcium-Rich Solution, J. Nucl. Mater. 435 (2013) 112–122, https://doi.org/10.1016/j.jnucmat.2012.12.032.
[13] B. Wild, et al., pH-dependent control of feldspar dissolution rate by altered surface layers, Chem. Geol. 442 (2016) 148–159, https://doi.org/10.1016/j.chemgeo.2016.08.035.
[14] M. Fournier, et al., Effect of pH on the stability of passivating gel layers formed on International Simple Glass, J. Nucl. Mater. 524 (2019) 21–38, https://doi.org/10.1016/j.jnucmat.2019.06.029.
[15] S. Gin, et al., The fate of silicon during glass corrosion under alkaline conditions: a mechanistic and kinetic study with the International Simple Glass, Geochim. Cosmochim. Ac. 151 (2015) 68–85, https://doi.org/10.1016/j.gca.2014.12.009.
[16] J.D. Vienna, J.J. Neeway, J.V. Ryan, S.N. Kerisit, Impacts of glass composition, pH, and temperature on glass forward dissolution rate, npj Mater. Degrad. 2 (2018) 22, https://doi.org/10.1038/s41529-018-0042-5.
[17] D.J. Backhouse, et al., Corrosion of the International Simple Glass under acidic to hyperalkaline conditions, npj Mater. Degrad. 2 (2018) 29, https://doi.org/10.1038/s41529-018-0050-5.
[18] S. Gin, et al., A general mechanism for gel layer formation on borosilicate glass under aqueous corrosion, J. Phys. Chem. C 124 (2020) 5132–5144.
[19] M. Fournier, S. Gin, P. Frugier, Resumption of nuclear glass alteration: state of the art, J. Nucl. Mater. 448 (2014) 348–363.
[20] H. Aréna, et al., Impact of Fe, Mg and Ca elements on glass alteration: interconnected processes, Geochim. Cosmochim. Ac. 239 (2018) 420–445, https://doi.org/10.1016/j.gca.2018.08.007.
[21] S. Liu, K. Ferrand, K. Lemmens, Transport- and surface reaction-controlled SON68 glass dissolution at 30 °C and 70 °C and pH=13.7, Appl. Geochem. 61 (2015) 302–311, https://doi.org/10.1016/j.apgeochem.2015.06.014.
[22] P. Jollivet, S. Gin, S. Schumacher, Forward dissolution rate of silicate glasses of nuclear interest in clay-equilibrated groundwater, Chem. Geol. 330–331 (2012) 207–217, https://doi.org/10.1016/j.chemgeo.2012.09.012.
[23] H. Maraghechi, F. Rajabipour, C.G. Pantano, W.D. Burgos, Effect of calcium on dissolution and precipitation reactions of amorphous silica at high alkalinity, Cement Concret. Res. 87 (2016) 1–13, https://doi.org/10.1016/j.cemconres.2016.05.004.
[24] B. Cagnon, D. Daval, M. Cabié, D. Lemarchand, S Gin, A comparative study of the dissolution mechanisms of amorphous and crystalline feldspars at acidic pH conditions, npj Mater. Degrad. 6 (2022) 34, https://doi.org/10.1038/s41529-022-00240-6.
[25] K. Damodaran, J.-M. Delaye, A.G. Kalinichev, S. Gin, Deciphering the non-linear impact of Al on chemical durability of silicate glass, Acta Mater. (2021) 117478, https://doi.org/10.1016/j.actamat.2021.117478.
[26] K. Damodaran, S. Gin, S. Narayanasamy, J.-M Delaye, On the effect of Al on alumino-borosilicate glass chemical durability, npj Mater. Degrad. 7 (2023) 46, https://doi.org/10.1038/s41529-023-00364-3.
[27] K. Ferrand, et al., Dissolution kinetics of international simple glass and formation of secondary phases at very high surface area to solution ratio in young cement water, Mater. (Basel) 14 (2021).
[28] H. Aréna, D. Rébiscoul, E. Garcès, N Godon, Comparative effect of alkaline elements and calcium on alteration of International Simple Glass, npj Mater. Degrad. 3 (2019) 10, https://doi.org/10.1038/s41529-019-0072-7.
[29] J.J. Neeway, et al., Acceleration of glass alteration rates induced by zeolite seeds at controlled pH, Appl. Geochem. 113 (2020) 104515, https://doi.org/10.1016/j.apgeochem.2019.104515.
[30] S. Mercado-Depierre, M. Fournier, S. Gin, F. Angeli, Influence of zeolite precipitation on borosilicate glass alteration under hyperalkaline conditions, J. Nucl. Mater. 491 (2017) 67–82, https://doi.org/10.1016/j.jnucmat.2017.04.043.
[31] C. Mann, et al., Influence of young cement water on the corrosion of the International Simple Glass, npj Mater. Degrad. 3 (2019) 5, https://doi.org/10.1038/s41529-018-0059-9.
[32] S. Garrault-Gauffinet, A. Nonat, Experimental investigation of calcium silicate hydrate (C-S-H) nucleation, J. Cryst Grow. 200 (1999) 565–574, https://doi.org/10.1016/S0022-0248(99)00051-2.
[33] N. Krautwurst, et al., Two-Step Nucleation Process of Calcium Silicate Hydrate, the Nanobrick of Cement, Chem. Mater. 30 (2018) 2895–2904, https://doi.org/10.1021/acs.chemmater.7b04245.
[34] N. Krautwurst, Nucleation of Calcium Silicate Hydrate in Aqueous Solution and the Influence of Biomolecules On Cement Hydration, Johannes Gutenberg-Universität, Dissertation, Mainz, 2017, p. 2017.
[35] Aretxabaleta, X., López-Zorrilla, J., Etxebarria, I. & Manzano, H. CSH nucleation pathway from atomistic simulations. (2023).
[36] P. Blanc, X. Bourbon, A. Lassin, E.C. Gaucher, Chemical model for cement-based materials: temperature dependence of thermodynamic functions for

nanocrystalline and crystalline C–S–H phases, Cement Concret. Res. 40 (2010) 851–866, https://doi.org/10.1016/j.cemconres.2009.12.004.
[37] P. Blanc, X. Bourbon, A. Lassin, E.C. Gaucher, Chemical model for cement-based materials: thermodynamic data assessment for phases other than C–S–H, Cement Concret. Res. 40 (2010) 1360–1374, https://doi.org/10.1016/j.cemconres.2010.04.003.
[38] X. Liu, et al., Carbonation behavior of calcium silicate hydrate (C-S-H): its potential for CO2 capture, Chem. Eng. J. 431 (2022) 134243, https://doi.org/10.1016/j.cej.2021.134243.
[39] B. Wu, G. Ye, Study of carbonation rate of synthetic CSH by XRD, NMR and FTIR, Heron 64 (2019) 21–38.
[40] A.E. Morandeau, C.E. White, In situ X-ray pair distribution function analysis of accelerated carbonation of a synthetic calcium–silicate–hydrate gel, J. Mater. Chem. A 3 (2015) 8597–8605, https://doi.org/10.1039/c5ta00348b.
[41] J. Chang, Y. Fang, Quantitative analysis of accelerated carbonation products of the synthetic calcium silicate hydrate(C–S–H) by QXRD and TG/MS, J. Therm. Anal. Calorim. 119 (2015) 57–62, https://doi.org/10.1007/s10973-014-4093-8.
[42] K. Garbev, et al., Structural features of C–S–H(I) and its carbonation in air—a Raman spectroscopic study. part I: fresh phases, J. Am. Ceram. Soc. 90 (2007) 900–907, https://doi.org/10.1111/j.1551-2916.2006.01428.x.
[43] L. Black, et al., Structural Features of C–S–H(I) and Its Carbonation in Air—A Raman Spectroscopic Study. Part II: carbonated Phases, J. Am. Ceram. Soc. 90 (2007) 908–917, https://doi.org/10.1111/j.1551-2916.2006.01429.x.
[44] T.F. Sevelsted, J. Skibsted, Carbonation of C–S–H and C–A–S–H samples studied by 13C, 27Al and 29Si MAS NMR spectroscopy, Cement Concret. Res. 71 (2015) 56–65, https://doi.org/10.1016/j.cemconres.2015.01.019.
[45] J. Li, Q. Yu, H. Huang, S. Yin, Effects of Ca/Si Ratio, Aluminum and Magnesium on the Carbonation Behavior of Calcium Silicate Hydrate, Mater. (Basel) 12 (2019).
[46] J.F. Young, R.L. Berger, J. Breese, Accelerated Curing of Compacted Calcium Silicate Mortars on Exposure to CO2, J. Am. Ceram. Soc. 57 (1974) 394–397, https://doi.org/10.1111/j.1151-2916.1974.tb11420.x.
[47] M. Fernández Bertos, S.J.R. Simons, C.D. Hills, P.J. Carey, A review of accelerated carbonation technology in the treatment of cement-based materials and sequestration of CO_2, J. Hazard. Mater. 112 (2004) 193–205, https://doi.org/10.1016/j.jhazmat.2004.04.019.
[48] S. Goto, K. Suenaga, T. Kado, M. Fukuhara, Calcium silicate carbonation products, J. Am. Ceram. Soc. 78 (1995) 2867–2872, https://doi.org/10.1111/j.1151-2916.1995.tb09057.x.
[49] J. van der Lee, L. De Windt, CHESS Tutorial and Cookbook. Updated for Version 3.0, 2002. Vol. Manual Nr. LHM/RD/02/13.
[50] P. Blanc, et al., ThermoChimie database developments in the framework of cement/clay interactions, Appl. Geochem. 55 (2015) 95–107, https://doi.org/10.1016/j.apgeochem.2014.12.006.
[51] N.C.M. Marty, et al., A database of dissolution and precipitation rates for clay-rocks minerals, Appl. Geochem. 55 (2015) 108–118, https://doi.org/10.1016/j.apgeochem.2014.10.012.
[52] M. Grivé, L. Duro, E. Colàs, E. Giffaut, Thermodynamic data selection applied to radionuclides and chemotoxic elements: an overview of the ThermoChimie-TDB, Appl. Geochem. 55 (2015) 85–94, https://doi.org/10.1016/j.apgeochem.2014.12.017.
[53] E. Giffaut, et al., Andra thermodynamic database for performance assessment: thermoChimie, Appl. Geochem. 49 (2014) 225–236, https://doi.org/10.1016/j.apgeochem.2014.05.007.
[54] J.V. Ryan, et al., ISG-2: properties of the second International Simple Glass, npj Mater. Degrad. 7 (2023) 47, https://doi.org/10.1038/s41529-023-00352-7.
[55] D. Daval, et al., Mechanism of wollastonite carbonation deduced from micro- to nanometer length scale observations, Am Miner. 94 (2009) 1707–1726, https://doi.org/10.2138/am.2009.3294.
[56] Zhakiyeva, Z. *Structure et dynamique de l'eau dans le ciment Portland et dans des ciments bas carbone*, (2021).
[57] B. Grambow, R. Muller, First-order dissolution rate law and the role of surface layers in glass performance assessment, J. Nucl. Mater. 298 (2001) 112–124.
[58] R.H. Doremus, Diffusion-controlled reaction of water with glass, J. Non Cryst. Solid. 55 (1983) 143–147, https://doi.org/10.1016/0022-3093(83)90014-5.
[59] W.L. Bourcier, D.W. Peiffer, K.G. Knauss, K.D. McKeegan, D.K. Smith, A kinetic model for borosilicate glass dissolution based on the dissolution affinity of a surface alteration layer, MRS Online Proceed. Lib. Arch. 176 (1989), https://doi.org/10.1557/PROC-176-209 null-null.
[60] R. Hellmann, The albite-water system .4. Diffusion modeling of leached and hydrogen-enriched layers, Geochim. Cosmochim. Ac. 61 (1997) 1595–1611.
[61] R. Hellmann, D. Tisserand, Dissolution kinetics as a function of the Gibbs free energy of reaction: an experimental study based on albite feldspar, Geochim. Cosmochim. Ac. 70 (2006) 364–383.
[62] R. Hellmann, et al., Unifying natural and laboratory chemical weathering with interfacial dissolution–reprecipitation: a study based on the nanometer-scale chemistry of fluid–silicate interfaces, Chem. Geol. 294–295 (2012) 203–216.
[63] S. Gin, et al., Dynamics of self-reorganization explains passivation of silicate glasses, Nat. Commun. 9 (2018) 2169.
[64] S. Gin, et al., Insights into the mechanisms controlling the residual corrosion rate of borosilicate glasses, npj Mater. Degrad. 4 (2020) 1–9.
[65] B. Grambow, A general rate equation for nuclear waste glass corrosion, Mater. Res. Soc. Symp. Proc. 44 (1985) 15–27.
[66] P. Aagaard, H.C. Helgeson, Thermodynamic and kinetic constraints on reaction-rates among minerals and aqueous-solutions .1. Theoretical considerations, Am. J. Sci. 282 (1982) 237–285.
[67] G. Berger, D. Beaufort, J.C. Lacharpagne, Experimental dissolution of sanidine under hydrothermal conditions: mechanism and rate, Am. J. Sci. 302 (2002) 663–685.
[68] D. Daval, et al., Influence of amorphous silica layer formation on the dissolution rate of olivine at 90 °C and elevated pCO(2), Chem. Geol. 284 (2011) 193–209, https://doi.org/10.1016/j.chemgeo.2011.02.021.
[69] D. Daval, R. Hellmann, G.D. Saldi, R. Wirth, K.G. Knauss, Linking nm-scale measurements of the anisotropy of silicate surface reactivity to macroscopic dissolution rate laws: new insights based on diopside, Geochim. Cosmochim. Ac. 107 (2013) 121–134, https://doi.org/10.1016/j.gca.2012.12.045.
[70] V. Daux, C. Guy, T. Advocat, J.L. Crovisier, P. Stille, Kinetic aspects of basaltic glass dissolution at 90 °C: role of aqueous silicon and aluminium, Chem. Geol. 142 (1997) 109–126.
[71] P. Frugier, et al., SON68 nuclear glass dissolution kinetics: current state of knowledge and basis of the new GRAAL model, J. Nucl. Mater. 380 (2008) 8–21, https://doi.org/10.1016/j.jnucmat.2008.06.044.
[72] P. Frugier, T. Chave, S. Gin, J.E. Lartigue, Application of the GRAAL model to leaching experiments with SON68 nuclear glass in initially pure water, J. Nucl. Mater. 392 (2009) 552–567, https://doi.org/10.1016/j.jnucmat.2009.04.024.
[73] P. Frugier, Y. Minet, N. Rajmohan, N. Godon, S Gin, Modeling glass corrosion with GRAAL, npj Mater. Degrad. 2 (2018) 35, https://doi.org/10.1038/s41529-018-0056-z.
[74] J.D. Vienna, J.V. Ryan, S. Gin, Y. Inagaki, Current Understanding and Remaining Challenges in Modeling Long-Term Degradation of Borosilicate Nuclear Waste Glasses, Int. J. Appl. Glass Sci. 4 (2013) 283–294, https://doi.org/10.1111/ijag.12050.
[75] S. Gin, Protective effect of the alteration gel: a key mechanism in the long-term behavior of nuclear waste glass, MRS Online Proceed. Libr. (OPL) 663 (2000) 207, https://doi.org/10.1557/proc-663-207.
[76] S. Gin, P. Frugier, SON68 glass dissolution kinetics at high reaction progress: experimental evidence of the residual rate, MRS Online Proceed. Lib. (OPL) 757 (2002), https://doi.org/10.1557/proc-757-ii5.9. II5.9.
[77] S. Gin, C. Jegou, P. Frugier, Y. Minet, Theoretical consideration on the application of the Aagaard-Helgeson rate law to the dissolution of silicate minerals and glasses, Chem. Geol. 255 (2008) 14–24, https://doi.org/10.1016/j.chemgeo.2008.05.004.
[78] M. Pollet-Villard, et al., Does crystallographic anisotropy prevent the conventional treatment of aqueous mineral reactivity? A case study based on K-feldspar dissolution kinetics, Geochim. Cosmochim. Ac. 190 (2016) 294–308, https://doi.org/10.1016/j.gca.2016.07.007.
[79] S. Ribet, S. Gin, Role of neoformed phases on the mechanisms controlling the resumption of SON68 glass alteration in alkaline media, J. Nucl. Mater. 324 (2004) 152–164, https://doi.org/10.1016/j.jnucmat.2003.09.010.
[80] M. Fournier, et al., Glass dissolution rate measurement and calculation revisited, J. Nucl. Mater. 476 (2016) 140–154.
[81] S.O. Merlino, Ca 10 Si 18 O 46 . 18H 2 O; the first example of a chain and sheet silicate, Am Miner. 68 (1983) 614–622.
[82] M. Fournier, S. Gin, P. Frugier, S. Mercado-Depierre, Contribution of zeolite-seeded experiments to the understanding of resumption of glass alteration, npj Mater. Degrad. 1 (2017) 17, https://doi.org/10.1038/s41529-017-0018-x.